



Contents lists available at ScienceDirect

Geochimica et Cosmochimica Acta

journal homepage: www.elsevier.com/locate/gca



Tin isotope heterogeneity and baseline of the upper continental crust

Jia-Xin She^{a,b}, Weiqiang Li^{a,b,*}, Edith Kubik^c, Frédéric Moynier^c, Xiang-Long Luo^{a,b}, Jun Mu^{a,b}, Shichao An^{a,b}, Chang-Zhi Wu^e, Zhongya Hu^f, Junfeng Ji^d

^a State Key Laboratory for Mineral Deposits Research, School of Earth Sciences and Engineering, Nanjing University, Nanjing, Jiangsu 210023, China

^b Frontiers Science Center for Critical Earth Material Cycling, Nanjing University, Nanjing, China

^c Université Paris Cité, Institut de Physique du Globe de Paris, CNRS, UMR 7154, F-75005 Paris, France

^d Ministry of Education Key Laboratory of Surficial Geochemistry, School of Earth Sciences and Engineering, Nanjing University, Nanjing, Jiangsu 210023, China

^e Key Laboratory of Western China's Mineral Resources and Geological Engineering, Ministry of Education, School of Earth Science and Resources, Chang'an University, Xi'an 710054, China

^f State Key Laboratory of Marine Geology, School of Ocean and Earth Science, Tongji University, Shanghai, China

ARTICLE INFO

Associate editor: Tomas Magna

Keywords:

Sn isotopes
UCC
Granites
Loess
Heterogeneity
Baseline

ABSTRACT

Stable Sn isotope ratios are emerging as a novel tracer for a wide range of geological processes; however, the Sn isotopic baseline of the upper continental crust (UCC) is not yet well-constrained. Here, we report high-precision Sn isotope data of a wide range of UCC samples, including granites, pegmatites, and sediments, to document the Sn isotopic composition of UCC. Significant variations in $\delta^{122/118}\text{Sn}_{3161a}$ (per mil deviation in $^{122}\text{Sn}/^{118}\text{Sn}$ relative to NIST 3161a) values are revealed for I-type ($\delta^{122/118}\text{Sn}_{3161a} = 0.025 \pm 0.026\text{‰}$ to $0.495 \pm 0.046\text{‰}$, $n = 20$) and S-type ($\delta^{122/118}\text{Sn}_{3161a} = 0.156 \pm 0.018\text{‰}$ to $0.501 \pm 0.075\text{‰}$, $n = 22$) granites. More extreme Sn isotope variability is observed for pegmatites, which have $\delta^{122/118}\text{Sn}_{3161a}$ from $0.256 \pm 0.047\text{‰}$ to $0.930 \pm 0.049\text{‰}$ ($n = 13$). The $\delta^{122/118}\text{Sn}_{3161a}$ of I-type granites decrease with decreasing TFe_2O_3 (total Fe as Fe_2O_3) and MgO contents and are attributed to the segregation of Fe-bearing minerals. Conversely, the Sn isotope variation of S-type granites appears to reflect source heterogeneity, whereas the Sn isotope variability of pegmatites may reflect fluid activity. In contrast, the loess samples display homogeneous $\delta^{122/118}\text{Sn}_{3161a}$ values ($0.132 \pm 0.034\text{‰}$ to $0.239 \pm 0.020\text{‰}$, $n = 20$) that show no correlation with the degree of chemical weathering, suggesting that loess is representative of the average Sn isotope composition of UCC. The $\delta^{122/118}\text{Sn}_{3161a}$ values of modern sediments and sedimentary rocks range from 0.080‰ to 0.490‰ ($n = 25$) and the Sn isotope variations may be related to chemical weathering or sediment provenance. Based on the lithology-weighted average $\delta^{122/118}\text{Sn}_{3161a}$ of UCC samples (41 granites and 45 sediments) in this study, the $\delta^{122/118}\text{Sn}_{3161a}$ value of UCC is estimated to be $0.233 \pm 0.099\text{‰}$, providing a reference point for further investigations. Tin is isotopically lighter in UCC compared to the mantle, owing to magmatic differentiation and crustal evolution processes.

1. Introduction

Tin is generally considered lithophile and chalcophile and behaves as a fluid-mobile element in the upper continental crust (Heinrich, 1990; Jochum et al., 1993; Lee, 2016; Witt-Eickschen et al., 2009; Yi et al., 1995). During mantle differentiation, Sn acts as a moderately incompatible element and is strongly enriched in the crust ($\sim 1.7 \mu\text{g/g}$ in the bulk crust) compared to the mantle ($0.12\text{--}0.17 \mu\text{g/g}$ in the primitive mantle) (Jochum et al., 1993; Rudnick and Gao, 2003; Sun and McDonough, 1989). High-temperature melting could also release Sn from

metamorphic rocks into crustal melts (Kunz et al., 2022; Romer and Kroner, 2016). Mobilization of Sn from sedimentary source rocks during subduction and metamorphism processes is a crucial mechanism of Sn enrichment in the crust (Romer et al., 2022), which results in the formation of giant Sn ore deposits in subduction-related settings (Sillitoe and Lehmann, 2021; Sun et al., 2012). Primary Sn ore deposits are invariably related to evolved felsic rocks (Lehmann, 2021). Tin has ten stable isotopes, which are found to fractionate significantly during various geological processes, including magma evolution and ore formation process (Sun et al., 2024; Wang et al., 2018; Yao et al., 2018).

* Corresponding author at: State Key Laboratory for Mineral Deposits Research, School of Earth Sciences and Engineering, Nanjing University, Nanjing, Jiangsu 210023, China.

E-mail address: liweiqiang@nju.edu.cn (W. Li).

<https://doi.org/10.1016/j.gca.2024.07.029>

Received 28 November 2023; Accepted 22 July 2024

Available online 27 July 2024

0016-7037/© 2024 Elsevier Ltd. All rights reserved, including those for text and data mining, AI training, and similar technologies.

Therefore, Sn and its isotopes hold the potential to trace crustal evolution and Sn cycling in subduction zones.

Stable Sn isotopes have been employed to study the planetary formation and evolution processes (Badullovich et al., 2017; Creech and Moynier, 2019; Kubik et al., 2021; Wang et al., 2018; Wang et al., 2019b; Wang et al., 2021b). Significant Sn isotope variations ($\sim 1\%$ in $\delta^{122/118}\text{Sn}_{3161a}$, per mil deviation in $^{122}\text{Sn}/^{118}\text{Sn}$ relative to NIST 3161a) occur in mantle-derived rocks, including peridotites (Wang et al., 2018), komatiites (Badullovich et al., 2017), basalts (Badullovich et al., 2017; She et al., 2023a; Wang et al., 2018), basaltic andesites and andesites (Badullovich et al., 2017). Tin isotopes are reported to be fractionated by redox processes (Roskosz et al., 2020), fractional crystallization (Badullovich et al., 2017), and partial melting processes (Wang et al., 2018). Compared to current knowledge of the Sn isotope composition of the mantle, little is known about the Sn isotope composition of the continental crust. To date, most Sn isotope studies focused on the investigation of mafic and ultramafic rocks, and knowledge of the Sn isotope signature of felsic rocks is limited to a few geological reference materials (GSP-2, JG-2, GSR-1, G-2, RGM-1) and granites from the Gejiu tin ore field, where $\delta^{122/118}\text{Sn}_{3161a}$ variations from 0.077‰ to 0.933‰ were observed (Creech et al., 2017; She et al., 2023b; Sun et al., 2024; Wang et al., 2022b). While recent study of Kubik et al. (2024) on diamicrites has provided the first robust estimate of $\delta^{122/118}\text{Sn}_{3161a}$ for the upper continental crust (UCC) at $0.220 \pm 0.140\%$, the stable Sn isotope compositions of UCC lithologies subjected to the magmatic-hydrothermal and surficial processes are still poorly characterized, a factor that severely limits the interpretations of the fast-growing Sn isotope data measured from various Sn ore deposits (Liu et al., 2021; Mason et al., 2020; Mathur et al., 2024; Powell et al., 2022; She et al., 2023c; Wang et al., 2019a; Wu et al., 2023; Yao et al., 2018; Zhou et al., 2022).

Therefore, the aims of this study are to: 1) Unravel the mechanisms of Sn isotope fractionation during magmatic-hydrothermal processes through a systematic investigation of granites of various archetypal classifications (I-type, S-type) and pegmatites representing the terminal stage of granite evolution; 2) Survey the Sn isotope signatures in loess samples and evaluate their suitability as the proxies of UCC; and 3) Investigate the Sn isotope composition of sediments subjected to diverse

surficial processes. To achieve these goals, we present a $\delta^{122/118}\text{Sn}_{3161a}$ dataset for 100 samples of various lithologies and geological backgrounds. Through meticulous analysis of UCC lithologies, we establish a new robust mean Sn isotope composition for UCC and compare this value with the current estimate of $\delta^{122/118}\text{Sn}_{3161a}$ of the Earth's mantle.

2. Samples

Samples investigated in this study include granites from Australia (36) and the Xinjiang province of China (6), Chinese pegmatites (13), loess (20), shales (2), modern sediments (18), and clastic sedimentary rocks (5). The locations of the samples are shown in Fig. 1.

2.1. Granites

2.1.1. Granites from the Lachlan Fold Belt, Australia

The I- and S-type granites were first defined in the Australian Paleozoic Lachlan Fold Belt (LFB) (Chappell and White, 1992). I-type granites are metaluminous and thought to originate from igneous sources without experiencing weathering cycles. The S-type granites are peraluminous, resulting from the partial melting of supracrustal sedimentary source material (Telus et al., 2012). The studied LFB granites have a wide range of chemical compositions with highly variable SiO_2 contents (Li et al., 2009; Telus et al., 2012). We analyzed 14 I-type granites (locality 9 in Fig. 1b) and 22 S-type granites (locality 10 in Fig. 1b) from the LFB. Most of the samples have been characterized before (Chappell and White, 1992; Kemp et al., 2008; Li et al., 2009; Telus et al., 2012) and used to constrain the Li, K, Cu, Zn, Mg, Fe, and U isotope compositions (Table S1) of the upper continental crust (Huang et al., 2020; Li et al., 2010; Li et al., 2009; Telus et al., 2012; Teng et al., 2004).

2.1.2. The Weiya Granites from Central Asian Orogenic Belt, NW China

The Central Asian Orogenic Belt is an orogenic belt between the Siberian Craton, the Tarim Craton, and the North China Craton (Kröner et al., 2008; Zhang et al., 2014). The Eastern Tianshan Orogenic Belt is located at the southwestern margin of the Central Asian Orogenic Belt (Han et al., 2018). The Weiya granitic ring complex in eastern Tianshan

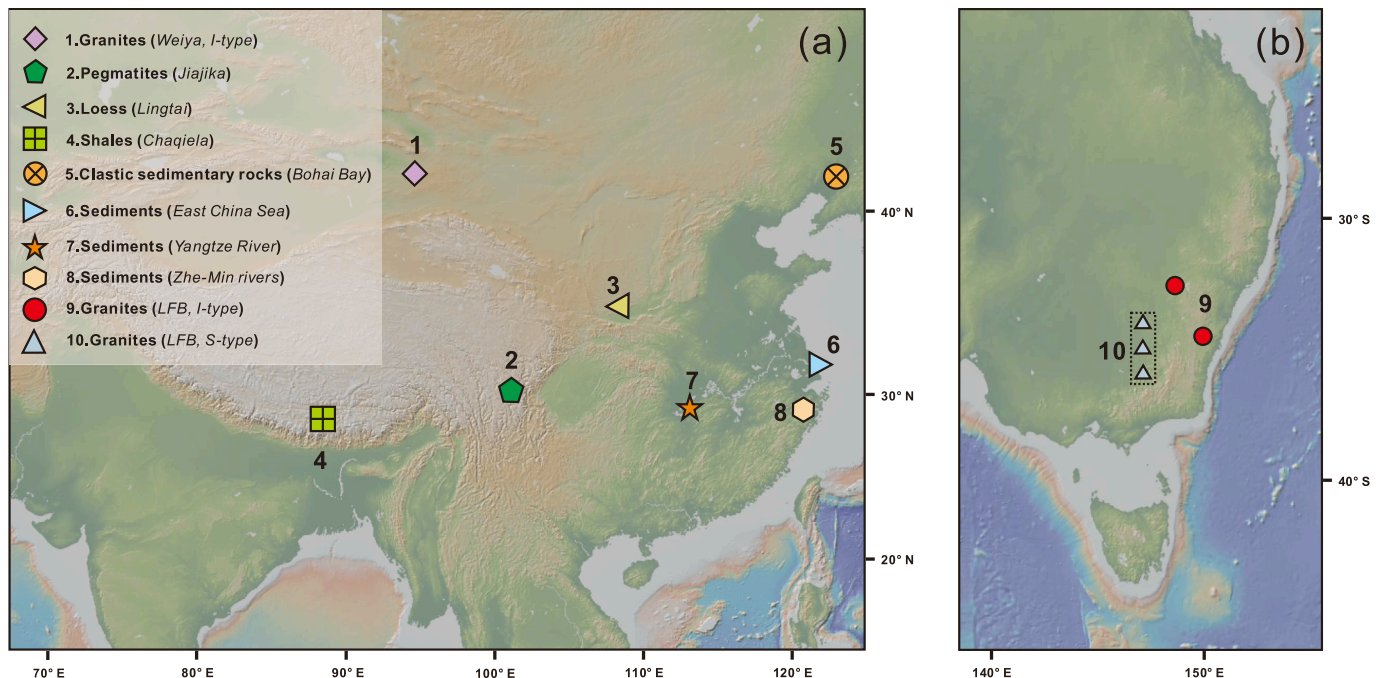


Fig. 1. The collection locations of samples from China (a) and Australia (b). “LFB” denotes the Lachlan Fold Belt in this and the subsequent figures.

is composed of quartz diorites, monzogranites, quartz syenites, quartz diorite porphyrites, and fine-grained granites from the central to the rim region, and these granites belong to the I-type (Zhang et al., 2008). Six samples from different segments of the Weiya complex (locality 1 in Fig. 1a) were analyzed for Sn isotope compositions.

2.2. Pegmatites from Jiajika, Songpan-Garze Orogenic belt, SW China

The Majingzi S-type granite pluton is situated southeast of the Jiajika dome, one of the large gneiss domes in the Songpan-Garze Orogenic Belt of southwest China (Xu et al., 2020). The borehole JSD-1 of the “Jiajika Scientific Drilling” (JSD) project is located northeast of the Majingzi granite (30°16′ 0.26″ N, 101°15′58.86″ E) (Xu et al., 2023). The pegmatites in JSD-1 core mainly comprise spodumene, tourmaline, biotite, muscovite, microcline, albite, garnet, and quartz (Luo et al., 2024; Zhou et al., 2023). Thirteen cassiterite-free pegmatite samples were collected from various depths along the 3-km JSD-1 borehole of the Jiajika scientific drilling project (locality 2 in Fig. 1a) and were analyzed for Sn isotope compositions.

2.3. Sediments

The Chinese Loess Plateau contains widespread, continuous, and thick Aeolian deposits in North China, and the loess-paleosol sequences of the Chinese Loess Plateau are excellent continental archives for the late Cenozoic (Balsam et al., 2004). The Lingtai section is one of the most complete sections on the Chinese Loess Plateau (Da et al., 2023; Ding et al., 1999). It consists of a complete Pleistocene loess-soil sequence with a thickness of ~175 m and Tertiary red clay deposits of ~130 m (Ding et al., 1999). Twenty loess samples were taken from the loess-paleosol sequences of the Lingtai section (locality 3 in Fig. 1a) for Sn isotope analysis.

Two shales from the Cretaceous Chaqiela section from southern Tibet, five clastic sedimentary rocks from the Eocene Shahejie formation (Sha3) in Bohai Bay of North China, as well as eighteen modern clastic sediments (from the East China Sea, Yangtze River, and Zhe-Min rivers) were collected and analyzed for Sn isotopes (Table S1).

The Chaqiela section (28°13′16.71″ N, 88°37′56.53″ E) is located in the east of Gamba County, southern Tibet. The Cretaceous strata of the Chaqiela section mainly comprise shales, siltstones, marls, and limestones (Zhang et al., 2016). The Gambadongshan Formation in the Chaqiela Formation (locality 4 in Fig. 1a) is characterized by black to grey shales (Fang et al., 2021), which were analyzed in this study.

The Damintun Depression is a Mesozoic and Cenozoic continental sag northeast of the Bohai Bay Basin, China (Chen et al., 2020). The Eocene Shahejie formation overlies the basement of the Damintun Depression and has four members (Sha1-Sha4) from the bottom to the top (Huang et al., 2021). The sandstone, siltstone, glutenite, and gritstone from the Shahejie formation (Sha3) in the Bohai Bay basin (locality 5 in Fig. 1a) were analyzed in this study.

The modern sediments analyzed in this study are from the East China Sea (5 samples, locality 6 in Fig. 1a), Yangtze River (9 samples, locality 7 in Fig. 1a), and suspended loads from the Zhe-Min rivers (4 samples, locality 8 in Fig. 1a). During the 2011 cruises, five surface sediment samples were collected from the shelf of the East China Sea. The surface sediments (1–2 cm) were taken using grab samplers and box cores. The Zhe-Min rivers are mountainous rivers that flow along the southeast coast of China into the East China Sea (Jian et al., 2020). The four suspended sediments were collected from four Zhe-Min rivers, including the Ou River, Feiyun River, Jiulong River, and Ling River, in 2012. The nine riverine sediments from the drainage basin of the Yangtze River were collected along the mainstream and tributary of the Yangtze River in 2021 and 2022.

3. Analytical methods

3.1. Whole-rock major and trace element analyses

The samples were crushed into ~200 mesh size using an agate mortar. The whole-rock elemental analyses were performed at the State Key Laboratory for Mineral Deposits Research, Nanjing University. Major element contents were measured using X-ray fluorescence spectrometry (XRF) with analytical uncertainty better than $\pm 0.5\%$ RSD. Trace element contents were determined using sector-field inductively coupled plasma mass spectrometry (ICP-MS) following sample digestion in pressurized Teflon bombs using a mixture of 29 M HF – 16 M HNO₃. Rhodium was used as an internal standard to monitor signal drift during ICP-MS analysis (Duan et al., 2021). The major and trace elements data for LFB granites and Jiajika pegmatites are taken from Kemp et al. (2008), Li et al. (2009), Telus et al. (2012), and Luo et al. (2024) (Table S1). It should be noted that Sn concentrations reported in this study are calculated by the isotope dilution method based on double-spike isotopic measurements as detailed in section 3.2.

3.2. Tin isotope analysis

The Sn isotope measurements for the majority of the samples were performed at Nanjing University following procedures reported in She et al., (2023b). Part of the granite samples were analyzed at the Institut de Physique du Globe de Paris (IPGP), France, using a similar method described in She et al., (2023a), and indicated in Table 1 and Table 2. In addition to the UCC samples, USGS reference materials (GSP-2, BCR-2, DST-2b, GSR-1, NOD-A-1, BHVO-2, AGV-2, RGM-2) were also processed and analyzed to monitor the accuracy of the analytical and instrumental approach (Table 1).

Approximately 20–1200 mg of rock powders (containing 1–2 μg Sn) were digested in tightly capped Teflon beakers with an 8 mL 1:1 mixture of 16 M HNO₃ – 29 M HF on a hotplate at 130 °C. The sample was mixed with a ¹¹⁷Sn-¹²²Sn double spike solution around the optimal spike-to-sample ratio of ~40:60 prior to sample digestion. Initial digestion lasted for two days to ensure equilibration of the isotope spike with the Sn dissolved from the rock powders. After complete sample digestion was verified by visual inspection, the solution was evaporated to dryness at 80 °C, re-dissolved in 6 mL aqua regia, and dried. After that, the sample was dissolved in 8 mL 8 M HCl to reflux at 130 °C for two days for decomposing fluorides. Then the sample was dried again, re-dissolved in 0.5 M HCl, and loaded on the column containing 1.5 mL pre-cleaned TRU resin for Sn purification (She et al., 2023b). Subsequently, the purified Sn fractions were dried at 80 °C and brought up in 0.3 M HNO₃ – 0.006 M HF.

Tin isotope analyses were performed by employing a Nu Sapphire multi-collector inductively coupled plasma mass spectrometer (MC-ICP-MS) housed at Nanjing University or a Thermo-Fischer Neptune Plus housed at IPGP (Table S2). The concentration of all Sn solutions was adjusted to 100 ng/mL before mass spectrometry. The typical signal intensity for ¹²⁰Sn was ~14 V per 100 ng/mL in Nanjing and ~20 V per 100 ng/mL at IPGP. During analysis, each sample was bracketed by a spiked NIST 3161a standard at the same concentration. All isotopic results are expressed in the $\delta^{122/118}\text{Sn}$ notation relative to the primary Sn isotopic reference solution NIST 3161a: $\delta^{122/118}\text{Sn}_{3161a} = \left[\frac{(^{122}\text{Sn}/^{118}\text{Sn})_{\text{sample}}}{(^{122}\text{Sn}/^{118}\text{Sn})_{3161a}} - 1 \right] \times 1000$, with errors reported as 2 standard deviations (2SD) of repeated analyses during an analytical session. The procedural blank of Sn is < 5.6 ng at Nanjing University and ~1.0 ng at IPGP, contributing to less than 0.3% of Sn in the analyzed samples. The intermediate (2SD external) precision is better than $\pm 0.069\%$ based on repeated analysis of GSP-2 (n = 12) at Nanjing University and GSP-2 (n = 9) at IPGP (Crech et al., 2017; She et al., 2023a; She et al., 2023b). The accuracy of Sn isotope analysis was verified by analyzing geological reference materials along with samples.

Table 1
Tin isotopic compositions of geological reference materials.

Standard	Type	Sn content ($\mu\text{g g}^{-1}$)	$\delta^{122/118}\text{Sn}_{3161a}$ (‰) ^a	2SD (‰)	N ^d	Method ^e
GSP-2 Replicate ^b Replicate Replicate Replicate Replicate Average^c (She et al., 2023a) (She et al., 2023b) (Wang et al., 2022)	Granite	6.35	0.209	0.053	3	Nanjing University IPGP
		6.26	0.246	0.05	4	
		6.31	0.19	0.012	4	
		6.59	0.231	0.012	2	
		6.48	0.234	0.011	2	
		6.25	0.246	0.017	2	
		6.64	0.239	0.013	2	
		6.41	0.228	0.042	7	
		6.57	0.224	0.069	9	
		6.52	0.223	0.029	12	
6.53	0.240	0.120	6			
BCR-2 Replicate Replicate Average (She et al., 2023a) (She et al., 2023b)	Basalt	2.27	0.319	0.010	2	Nanjing University IPGP
		2.21	0.296	0.014	2	
		2.23	0.273	0.011	2	
		2.24	0.296	0.046	3	
		2.06	0.284	0.038	16	
2.22	0.312	0.035	9			
DST-2b Replicate Average	Dunite	0.50	0.276	0.008	2	Nanjing University
		0.56	0.286	0.009	2	
		0.53	0.281	0.014	2	
GSR-1 Replicate Replicate Average (She et al., 2023b)	Granite	11.68	0.218	0.025	3	Nanjing University
		11.90	0.248	0.036	3	
		11.82	0.189	0.04	4	
		11.80	0.218	0.059	3	
		11.78	0.229	0.037	5	
NOD-A-1 Replicate Average (She et al., 2023b) (Wang et al., 2022)	Marine sediment	3.34	0.318	0.062	4	Nanjing University
		3.28	0.287	0.047	4	
		3.31	0.303	0.044	2	
		3.36	0.329	0.040	2	
		3.03	0.280	0.040	3	
BHVO-2 (She et al., 2023a) BHVO-2 (Wang et al., 2022)	Basalt	1.81	0.331	0.066	12	IPGP
		1.81	0.380	0.140	6	
AGV-2 (She et al., 2023a) AGV-2 (Wang et al., 2022)	Andesite	2.23	0.297	0.006	2	IPGP
		2.01	0.260	0.060	5	

Table 1 (continued)

Standard	Type	Sn content ($\mu\text{g g}^{-1}$)	$\delta^{122/118}\text{Sn}_{3161a}$ (‰) ^a	2SD (‰)	N ^d	Method ^e
RGM-2 (She et al., 2023a)	Rhyolite	4.31	0.152	0.051	2	IPGP

^a Tabulated data are averages of repeat measurements.

^b Replicate in this table represents full procedural repeats, including sample dissolution, column chemistry, and instrumental measurement.

^c The average and 2SD in bold indicate the average and 2SD of sample replicates.

^d N in this table represents the number of repeat measurements in one session or the number of sample replicates for data in bold.

^e The geological reference materials in this table are analyzed at Nanjing University and IPGP, which are labeled as “Nanjing University” and “IPGP,” respectively.

4. Results

The Sn isotope compositions of USGS reference materials from IPGP were reported before (She et al., 2023a) and listed in Table 1 (labeled IPGP). The reference materials measured at Nanjing University (labeled as Nanjing University) yielded $\delta^{122/118}\text{Sn}_{3161a}$ values (Table 1) consistent with literature data (She et al., 2023a; She et al., 2023b; Wang et al., 2022b), with $0.228 \pm 0.042\text{‰}$ ($n = 7$) for GSP-2 (granite), $0.296 \pm 0.046\text{‰}$ ($n = 3$) for BCR-2 (basalt), $0.218 \pm 0.059\text{‰}$ ($n = 3$) for GSR-1 (granite), and $0.303 \pm 0.044\text{‰}$ ($n = 2$) for NOD-A-1 (marine sediment). The Sn isotope composition of DST-2b (dunite) is reported here for the first time, which is $0.281 \pm 0.014\text{‰}$ in $\delta^{122/118}\text{Sn}_{3161a}$ ($n = 2$). The $\delta^{122/118}\text{Sn}_{3161a}$ of UCC samples, including duplicates and replicates investigated in this study, are listed in Tables 2–4 and S1. Overall, the studied samples have highly variable $\delta^{122/118}\text{Sn}_{3161a}$ values, ranging from $0.025 \pm 0.069\text{‰}$ to $0.930 \pm 0.069\text{‰}$ (Fig. 2).

4.1. Granites

The $\delta^{122/118}\text{Sn}_{3161a}$ values of granitic rocks range from $0.025 \pm 0.026\text{‰}$ to $0.501 \pm 0.075\text{‰}$ (Table 2). The Sn isotope compositions of S-type and I-type granites overlap (Fig. 2) and their mean Sn isotope composition is $0.265 \pm 0.203\text{‰}$ in $\delta^{122/118}\text{Sn}_{3161a}$.

The I-type granites exhibit large variations in chemical compositions, with highly variable SiO_2 (51.5–73.1 wt%), TFe_2O_3 (total Fe as Fe_2O_3) (1.68–10.5 wt%), TiO_2 (0.23–1.42 wt%), and MgO (0.32–6.09 wt%) contents (Table 2, S1; Fig. S1). The Sn contents range from 0.97 to 6.16 $\mu\text{g/g}$ for the LFB I-type granites and from 2.10 to 4.00 $\mu\text{g/g}$ for the Weiya I-type granites (Figs. 3 and 4). The Sn contents of I-type granites exhibit a positive correlation with SiO_2 contents and Ba/Sr ratios, whereas it inversely correlates with the concentrations of TFe_2O_3 , and MnO contents (Table S1). The Ba contents (154–915 $\mu\text{g/g}$) increase and Sr contents (148–580 $\mu\text{g/g}$) decrease with increasing SiO_2 contents for LFB I-type granites (Table S1; Fig. S1). The Ba (434–877 $\mu\text{g/g}$) and Sr (185–574 $\mu\text{g/g}$) contents of Weiya I-type granites decrease with increasing SiO_2 contents (Table S1; Fig. S1). The LFB I-type granites have $\delta^{122/118}\text{Sn}_{3161a}$ values varying from $0.025 \pm 0.026\text{‰}$ to $0.495 \pm 0.046\text{‰}$, with an average of $0.237 \pm 0.225\text{‰}$. In contrast, the Weiya granites have a more limited range of $\delta^{122/118}\text{Sn}_{3161a}$ values ($0.055 \pm 0.011\text{‰}$ to $0.222 \pm 0.004\text{‰}$) with an average of $0.170 \pm 0.133\text{‰}$ (Fig. 2). The $\delta^{122/118}\text{Sn}_{3161a}$ values of I-type granites display a positive trend with increasing concentrations of TiO_2 , TFe_2O_3 , and MgO , and a negative trend with decreasing SiO_2 content (Figs. 3 and 5).

The 23 LFB S-type granites have SiO_2 contents ranging from 65.8 to 74.1 wt%, MgO contents ranging from 0.03 to 3.94 wt%, and TiO_2 contents ranging from 0.05 to 0.83 wt% (Table 2, S1; Fig. 3, S1), with alumina saturation index (A/CNK, defined as the molar ratio of $\text{Al}_2\text{O}_3/$

Table 2

Tin isotopic compositions of granites from China and Australia investigated in this study.

Sample	Granite type	SiO ₂ (wt%) ^a	TFe ₂ O ₃ (wt%) ^a	MgO (wt%)	TiO ₂ (wt%)	Al ₂ O ₃ (wt%)	Sn (μg g ⁻¹)	δ ^{122/118} Sn _{3161a} (‰)	2SD (‰)	N ^d	Method ^e
Lachlan Fold Belt granites											
AB195	I-type	65.27	4.91	2.01	0.58	15.22	3.00	0.241	0.004	2	IPGP
AB6	I-type	67.39	4.94	1.72	0.53	14.48	4.00	0.204	0.027	2	IPGP
TKTH-1	I-type	63.50	8.91	2.38	0.81	15.95	1.80	0.232	0.011	2	IPGP
NB16	I-type	73.06	1.79	0.32	0.23	14.11	6.16	0.025	0.026	3	
Duplicate ^b								0.015	0.047	4	
Replicate ^c								0.040	0.044	3	
NB21	I-type	61.35	6.73	3.03	0.63	15.37	2.20	0.275	0.031	4	
NB27	I-type	58.02	8.24	3.82	0.74	16.30	1.76	0.318	0.053	3	
NB29	I-type	61.16	6.76	3.09	0.64	15.16	2.20	0.246	0.039	3	
Replicate								0.243	0.069	3	
NB33	I-type	57.90	8.22	4.04	0.76	15.62	1.99	0.296	0.024	3	
ZB2	I-type	57.48	7.65	2.76	0.63	17.02	1.42	0.323	0.052	4	
ZB4	I-type	65.80	4.57	1.22	0.49	15.22	1.64	0.115	0.028	4	
ZB7	I-type	64.49	4.92	1.84	0.41	15.89	1.00	0.111	0.049	4	
ZB8	I-type	64.63	4.92	1.82	0.42	15.72	0.97	0.186	0.050	4	
ZB129	I-type	58.23	8.46	3.90	1.38	14.83	1.66	0.247	0.067	3	
ZB135	I-type	51.52	10.45	6.09	1.42	15.46	1.06	0.495	0.046	4	
TKSB1	S-type	70.81	3.43	0.99	0.47	14.05	9.75	0.303	0.036	3	IPGP
BB6	S-type	66.03	5.59	3.94	0.52	13.96	5.27	0.209	0.006	2	IPGP
KB32	S-type	67.68	5.16	2.22	0.64	14.70	6.41	0.195	<0.001	2	IPGP
HV1	S-type	68.05	4.83	2.05	0.61	14.41	5.19	0.449	0.041	2	IPGP
BB1	S-type	70.81	3.43	0.99	0.47	14.05	4.61	0.184	0.011	2	IPGP
TKVT3	S-type	68.20	4.59	1.48	0.68	15.24	4.41	0.250	0.021	2	IPGP
S1	S-type	72.00	4.46	1.76	0.54	13.72	1.90	0.280	0.003	2	IPGP
VB1	S-type	68.35	4.20	1.84	0.62	14.62	6.83	0.257	0.066	4	
VB3	S-type	70.44	3.37	1.49	0.47	14.62	7.26	0.196	0.025	4	
VB4	S-type	67.87	4.76	2.05	0.71	14.72	6.30	0.188	0.032	3	
Replicate								0.173	0.044	4	
VB17	S-type	70.39	3.29	1.13	0.51	14.34	8.25	0.416	0.016	3	
VB21 ^f	S-type	74.13	0.75	0.03	0.05	14.52	20.15	0.501	0.075	3	
VB30	S-type	66.06	5.66	2.57	0.83	15.08	3.55	0.263	0.068	4	
VB32	S-type	69.60	4.24	1.38	0.67	14.25	6.97	0.358	0.065	3	
VB37	S-type	69.19	4.07	1.79	0.57	14.57	7.51	0.156	0.018	4	
VB38	S-type	65.78	5.44	2.39	0.80	15.46	6.07	0.326	0.051	3	
VB39	S-type	67.05	5.12	2.21	0.77	14.70	5.44	0.329	0.055	4	
VB65	S-type	67.71	4.49	2.03	0.65	14.96	5.60	0.172	0.057	4	
replicate								0.162	0.067	4	
VB99	S-type	69.63	3.28	1.60	0.46	14.70	11.19	0.329	0.050	3	
VB140	S-type	72.48	1.77	0.47	0.25	14.50	22.95	0.270	0.060	4	
VB143	S-type	70.55	3.48	1.33	0.49	14.47	9.54	0.304	0.027	4	
VB160	S-type	71.07	3.24	1.19	0.47	14.28	14.39	0.293	0.042	3	
Weiya granites											
19KH-185	I-type	70.77	2.44	0.95	0.35	14.44	2.90	0.136	0.014	2	IPGP
19KH-189	I-type	72.58	1.68	0.47	0.24	14.32	4.00	0.168	0.010	2	IPGP
19KH-191	I-type	61.95	4.88	2.65	0.81	16.67	2.80	0.209	0.013	2	IPGP
19KH-193	I-type	61.70	4.96	2.69	0.80	16.77	2.70	0.230	0.010	2	IPGP
19KH-197	I-type	71.98	1.98	0.56	0.24	14.35	2.80	0.055	0.011	2	IPGP
19KH-201	I-type	63.60	4.65	2.36	0.84	16.34	2.10	0.222	0.004	2	IPGP

^a The major elements are from Kemp et al. (2008), Li et al. (2009), and Telus et al. (2012). TFe₂O₃ in this and the following tables denotes total Fe as Fe₂O₃.

^b Duplicate in this table represents repeat measurements on the same purified solution during different sessions.

^c Replicate in this table represents full procedural repeats, including sample dissolution, column chemistry, and instrumental measurement.

^d N in this table represents the number of repeat measurements in one session.

^e The samples in this and the following are analyzed at Nanjing University except for those labeled as “IPGP,” which were analyzed at IPGP.

^f This sample was affected by fluid activity.

(CaO + Na₂O + K₂O) > 1.1 (Fig. S2). The Sn contents of the S-type granites are also variable, ranging from 1.90 to 22.95 μg/g (Figs. 3, 4). The Sn concentrations of S-type granites increase with higher Rb/Sr ratios, while they decrease with increasing TiO₂, TFe₂O₃, Sr, Ni contents, and K/Rb ratios (Table S1). The Ba (21–1015 μg/g) and Sr (39–186 μg/g) contents of the studied S-type granites decrease with increasing SiO₂ contents (Table S1; Fig. S1). The Cr contents of S-type granites decrease linearly with increasing SiO₂ contents (Fig. S1). The S-type granites have δ^{122/118}Sn_{3161a} values that vary from 0.156 ± 0.018‰ to 0.501 ± 0.075‰, displaying no discernible correlation with common indices of magma differentiation (Table 2; Fig. 3). The average δ^{122/118}Sn_{3161a} values of S-type granites is 0.283 ± 0.183‰.

4.2. Pegmatites

The Jiajika pegmatites have variable SiO₂ contents (64.2–78.5 wt%), MgO contents (0.03–2.25 wt%), TiO₂ contents (<0.45 wt%), and TFe₂O₃ contents (0.20–5.30 wt%) (Table 3, S1; Fig. 3, S1). They have Sn contents ranging from 4.24 μg/g to 63.77 μg/g (Table 3; Figs. 3 and 4), and their Ba (1–103 μg/g) and Sr (8–52 μg/g) contents are also variable (Table S1; Fig. S1). The Jiajika pegmatites show significant variability in δ^{122/118}Sn_{3161a} ranging from 0.256 ± 0.047‰ to 0.930 ± 0.049‰ (Table 3; Fig. 2). The Jiajika pegmatites display significantly heavier Sn isotope compositions compared to other UCC materials investigated in this study. There is no obvious correlation between Sn isotope composition and SiO₂ or other major elements for the studied pegmatites

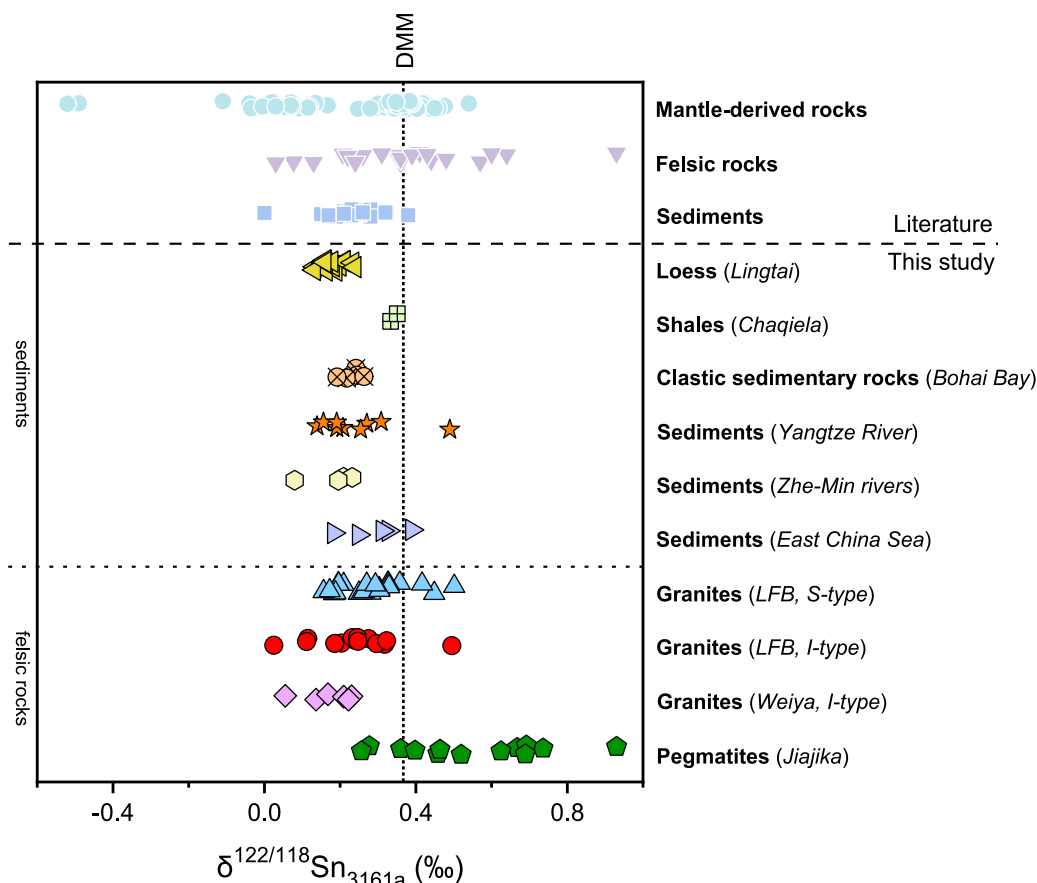


Fig. 2. Summary of $\delta^{122/118}\text{Sn}_{3161a}$ for samples investigated in this study and from literature (Badullovich et al., 2017; Creech et al., 2017; Kubik et al., 2024; She et al., 2023a; Sun et al., 2024; Wang et al., 2018; Wang et al., 2022). The data of Badullovich et al. (2017) here and below are converted into $\delta^{122/118}\text{Sn}_{3161a}$ by assuming an identical $\delta^{122/118}\text{Sn}_{3161a}$ of BHVO-2 in Badullovich et al. (2017) and She et al., (2023b). The Sn isotope composition of the Depleted MORB Mantle (DMM) is from She et al., (2023a). The $\delta^{122/118}\text{Sn}_{3161a}$ data along with the uncertainties (2SD) from this study are displayed in Tables 2-4 for this and the following figures.

(Table 3; Figs. 3 and 5).

4.3. Sediments

The Lingtai loess samples from the Chinese Loess Plateau have SiO_2 and Al_2O_3 contents ranging from 56.0 to 65.4 wt% and 12.3 to 15.7 wt %, respectively (Table 4, S1). Their Sn contents are relatively homogeneous (2.31–3.30 $\mu\text{g/g}$). The $\delta^{122/118}\text{Sn}_{3161a}$ values of loess are also highly homogeneous regardless of the depositional ages, falling in a narrow range from $0.132 \pm 0.034\text{‰}$ to $0.239 \pm 0.020\text{‰}$ (Table 4) despite the variable depositional environments and depths. The average $\delta^{122/118}\text{Sn}_{3161a}$ of all loess samples is $0.177 \pm 0.059\text{‰}$ (2SD, $n = 20$).

The sedimentary rocks and modern sediments have a wide range of SiO_2 (52.2–79.9 wt%), Al_2O_3 (5.00–16.6 wt%), and TiO_2 contents (0.14–1.47 wt%) (Table 4, S1). The chemical index of alteration (CIA) is defined as molar $\text{Al}_2\text{O}_3/(\text{Al}_2\text{O}_3 + \text{CaO}^* + \text{Na}_2\text{O} + \text{K}_2\text{O})$, where CaO^* refers to CaO bound in silicate phases, and is usually used to assess the degree of chemical weathering (McLennan, 1993; Nesbitt and Young, 1982). The sedimentary rocks and modern sediments studied here show a wide range of CIA values between 51.9 and 73.3 (Table 4). The Sn contents of these samples range from 0.84 $\mu\text{g/g}$ to 18.34 $\mu\text{g/g}$ (Table 4; Fig. 4). Two shale samples from Tibet and five clastic sedimentary rocks from the Bohai Bay Basin show a $\delta^{122/118}\text{Sn}_{3161a}$ variation from $0.333 \pm 0.069\text{‰}$ to $0.351 \pm 0.027\text{‰}$ and from $0.192 \pm 0.058\text{‰}$ to $0.263 \pm 0.042\text{‰}$, respectively (Table 4; Fig. 2). The modern sediments from East China Sea, Yangtze River, and Zhe-Min rivers show considerable variation in $\delta^{122/118}\text{Sn}_{3161a}$, ranging between $0.080 \pm 0.012\text{‰}$ and $0.490 \pm$

0.019‰ (Table 4; Fig. 2), with an average of $0.243 \pm 0.193\text{‰}$.

5. Discussion

The $\delta^{122/118}\text{Sn}_{3161a}$ values of the investigated samples display significant variations ($0.025 \pm 0.026\text{‰}$ to $0.930 \pm 0.049\text{‰}$), indicating that UCC is highly heterogeneous regarding its Sn isotope compositions, providing evidence of Sn isotope fractionation within UCC. Below, the Sn isotope variations of different sample sets are evaluated, followed by the estimation of the average $\delta^{122/118}\text{Sn}_{3161a}$ value for UCC.

5.1. Tin isotope fractionation in evolved magmatic rocks

5.1.1. I-type granites

The exposed crystalline upper continental crust is predominantly composed of granitic rocks (Taylor and McLennan, 1985). Granites can be formed by various processes, including fractional crystallization, crustal assimilation, magma mixing, and melt-residue segregation (Brown, 2013). Although previous studies found a correlation between Sn isotope ratios and SiO_2 contents for geological reference materials (GSP-2, AGV-2, BCR-2, BHVO-2) (Creech et al., 2017), these samples were not genetically linked. The Sn isotope data of granites reported in this study provide an opportunity to assess the effect of magmatic differentiation on Sn isotope fractionation. This is because the Weiya and LFB I-type granites have $\text{Nb/Ta} > 5$ (Fig. 6b), $\text{K/Rb} > 100$ (Fig. S1e), and $\text{Zr/Hf} > 26$ (Table S1), as well as limited variation of Rb/Th (Fig. 6a) and U/Th (Fig. 5d). These chemical indices are well within the range of

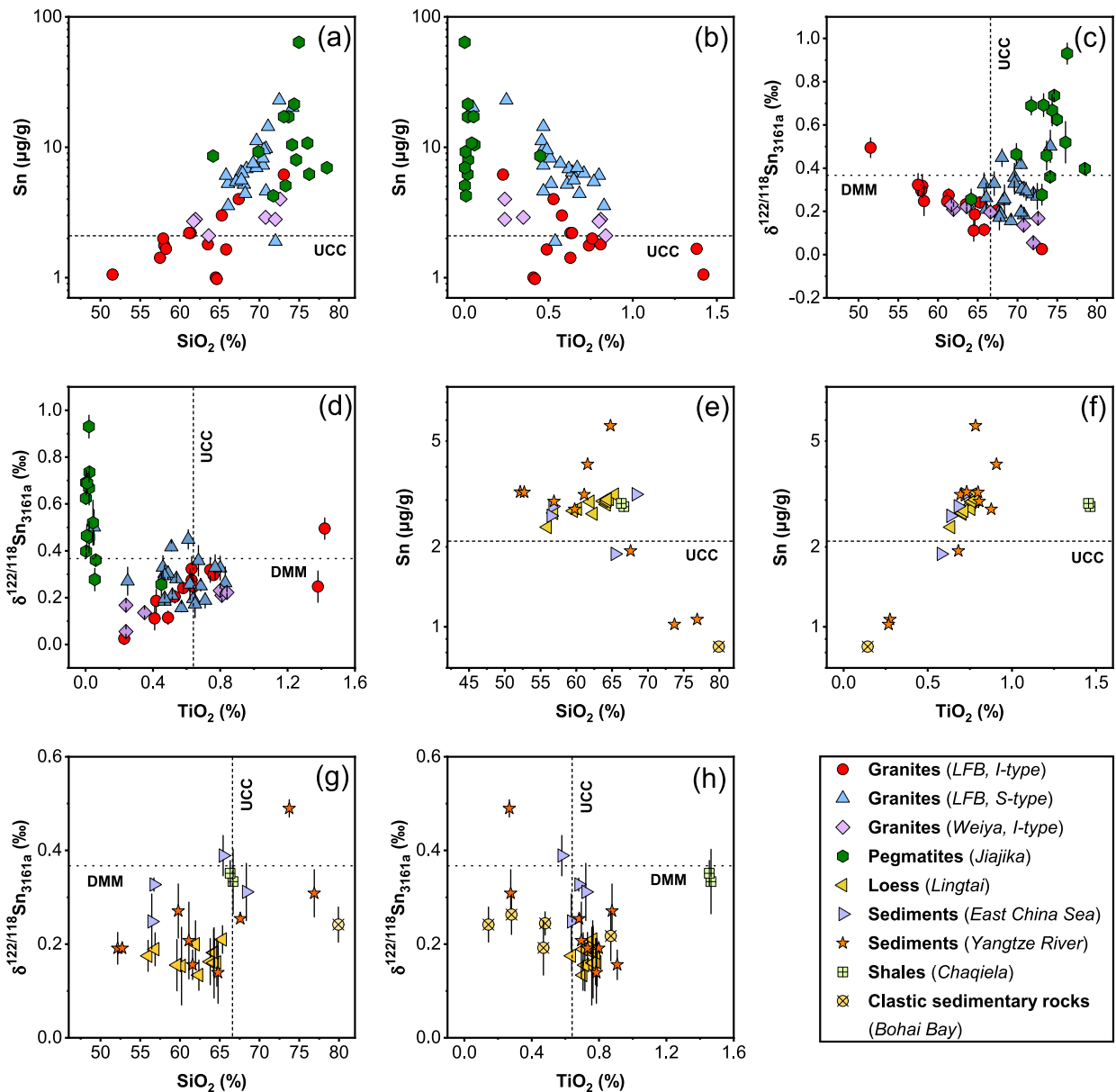


Fig. 3. Plots of (a) Sn ($\mu\text{g/g}$) vs. SiO_2 (wt%), (b) Sn ($\mu\text{g/g}$) vs. TiO_2 (wt%), (c) $\delta^{122/118}\text{Sn}_{3161a}$ vs. SiO_2 (wt%), (d) $\delta^{122/118}\text{Sn}_{3161a}$ vs. TiO_2 (wt%) for granites and pegmatites, (e) Sn ($\mu\text{g/g}$) vs. SiO_2 (wt%), (f) Sn ($\mu\text{g/g}$) vs. TiO_2 (wt%), (g) $\delta^{122/118}\text{Sn}_{3161a}$ vs. SiO_2 (wt%), (h) $\delta^{122/118}\text{Sn}_{3161a}$ vs. TiO_2 (wt%) for sediments analyzed in this study. Error bars in the figures represent two standard deviations (2SD) of $\delta^{122/118}\text{Sn}_{3161a}$. The elemental compositions of the upper continental crust (UCC) are from Rudnick and Gao, (2003). The Sn isotope composition of the depleted MORB mantle (DMM) is from She et al., (2023a).

typical magmatic granitic rocks (Bali et al., 2011; Ballouard et al., 2016; Bau, 1996; Irber, 1999; Nan et al., 2018; Wu et al., 2017). The $\delta^{122/118}\text{Sn}_{3161a}$ values of I-type granites display no correlations with U/Th and Rb/Th ratios (Fig. 5d, 6a), which are also sensitive indicators of hydrothermal activity in magmatic systems (Bali et al., 2011; Nan et al., 2018). Therefore, magmatic-hydrothermal interaction cannot account for the observed Sn isotope variations of Weiya and LFB I-type granites.

Fractional crystallization of minerals plays a major role in magma differentiation and may be the prominent cause for the observed Sn isotope variation of I-type granites. There are obvious correlations between SiO_2 and other major elements, such as MgO, TFe_2O_3 , and TiO_2 contents for I-type granites from LFB and Weiya (Table 2; Fig. S1). The Ba, Nb, Pb, and Rb contents for most LFB I-type granites and Eu, Sr, and TiO_2 contents of most Weiya I-type granites are depleted relative to upper crust values (Table S1; Fig. 3, S1), suggesting that they underwent various extents of fractional crystallization. The Ba/Sr ratios and Ba contents decline sharply with increasing Sr contents, implying

segregation of biotite (Fig. S1h, i), because Ba is compatible in biotite and K-feldspar, while Sr has high partition coefficients in K-feldspar and plagioclase relative to melt (Hanson, 1978; Wu et al., 2003). The V and Sc contents of the I-type granites are positively correlated (Fig. S3a), indicating fractional crystallization of Fe-bearing minerals including Fe-Ti oxides, amphibole, and biotite, in which V and Sc are compatible (Adam and Green, 2006; Bea et al., 1994; Klemme et al., 2006; Luhr and Carmichael, 1980). As shown in Fig. 5a, b, the $\delta^{122/118}\text{Sn}_{3161a}$ values of LFB and Weiya I-type granites decrease with declining MgO and TFe_2O_3 contents, implying the removal of isotopically heavy Sn by segregation of Fe-bearing minerals during magma evolution.

The mineral/melt partition coefficients for Sn were estimated to be 0.046 for K-feldspar (Larsen, 1979), 0.94–1.27 for plagioclase (Badulovich et al., 2017), 0.01–5.55 for biotite (Wei et al., 2024), 0.08–12.66 for amphibole (Adam and Green, 2006; Wei et al., 2024), 0.03–69.5 for ilmenite (Huang et al., 2024; Klemme et al., 2006; Wei et al., 2024) and 1.34–108.43 for magnetite (Wei et al., 2024). Tin can partition strongly

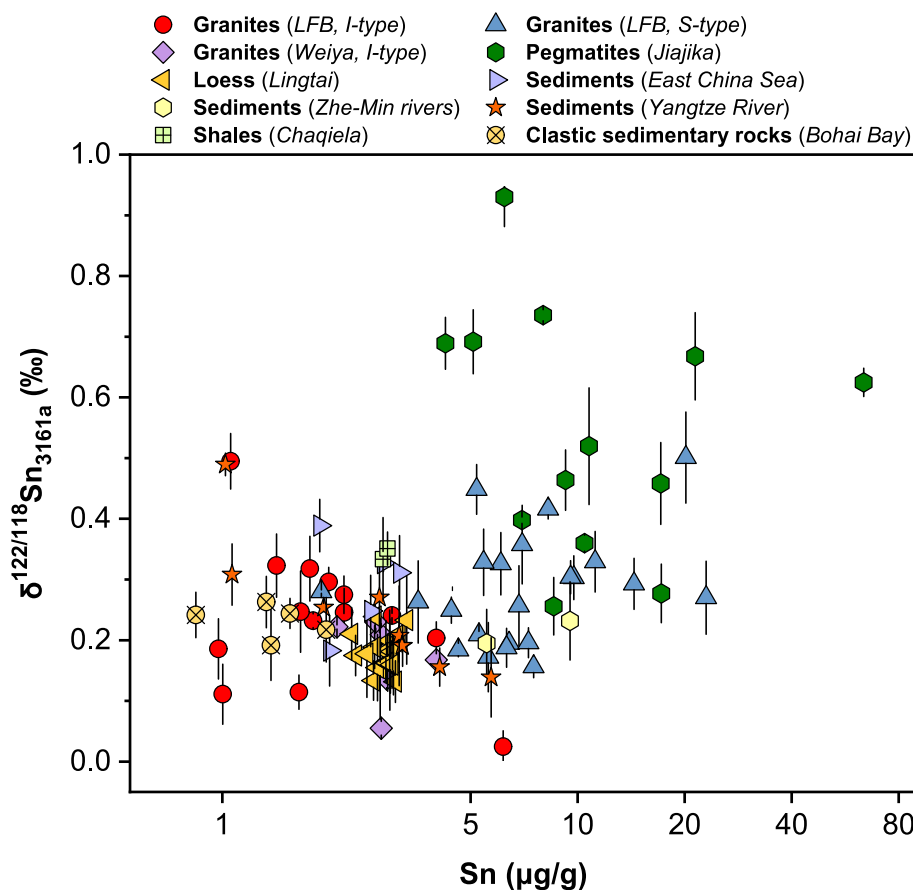


Fig. 4. Plot of $\delta^{122/118}\text{Sn}_{3161a}$ values versus Sn ($\mu\text{g/g}$) contents for samples analyzed in this study.

into cassiterite (Wu et al., 2023), and the presence of cassiterite with highly variable Sn isotope compositions (Berger et al., 2018; Berger et al., 2019; Brugmann et al., 2017; Mason et al., 2020; Mason et al., 2016; Mathur et al., 2024; Powell et al., 2022; She et al., 2023c; Wang et al., 2019a; Wu et al., 2023; Yao et al., 2018) in granites could cause Sn isotopic anomaly of bulk rock samples. However, no cassiterite has been identified for samples from LFB and Weiya. Therefore, the behavior of Sn and its isotopes in I-type granites are likely controlled by plagioclase, biotite, amphibole, and Fe-Ti oxides (magnetite, ilmenite). The $\delta^{122/118}\text{Sn}_{3161a}$ values do not correlate with contents of feldspar-compatible elements like Ba, Rb, and Sr, as well as Rb/Sr ratios (Table S1; Fig. 5), indicating that fractional crystallization of feldspar does not affect the Sn isotope compositions of I-type granites. Tin is present mainly in two oxidation states (Sn^{2+} , Sn^{4+}), and Sn^{4+} is more compatible in minerals such as biotite, amphibole and Fe-Ti oxides in granitic rocks following substitution of Sn^{4+} for Ti^{4+} , Fe^{3+} , Al^{3+} (Chen et al., 2022; Farges et al., 2006; Klemme et al., 2006; Wang et al., 2013; Yuan et al., 2018), while Sn^{2+} is preferentially accommodated in granitic melts (Taylor and Wall, 1992). Besides, Sn^{4+} is likely to have a lower coordination number in minerals compared to melt with various redox states (Badullovich et al., 2017; Dulnee et al., 2013; Farges et al., 2006; Wang et al., 2018). Tin sites with higher oxidation state, lower coordination number, and shorter bond length favor heavier isotopes (Roskosz et al., 2020; Sun et al., 2023; Wang et al., 2023). Therefore, Fe-Ti oxides, biotite, and amphibole tend to enrich heavier Sn isotopes compared to silicate melts. The decreasing $\delta^{122/118}\text{Sn}_{3161a}$ values of I-type granites with decreasing MgO and TFe_2O_3 contents (Fig. 5a, b) can thus be explained by preferential incorporation of heavy Sn isotopes into Fe-Ti oxides, biotite, and amphibole.

5.1.2. S-type granites

The Rb/Sr ratios and Ba contents of S-type granites correlate with Sr contents, suggesting crystallization of feldspar (Fig. S1f, i). The lack of correlation between $\delta^{122/118}\text{Sn}_{3161a}$ and Rb/Sr, Ba, Sr, SiO_2 , and Fe_2O_3 contents (Table S1; Figs. 3, 5) indicates that magmatic evolution is not the primary control of the Sn isotope compositions of the LFB S-type granites. Crystallization of feldspar will lower the Eu/Eu^* (chondrite-normalized $\text{Eu}/\sqrt{(\text{Sm} \times \text{Gd})}$) of residual melts (Holder et al., 2020; Wang et al., 2022a). A high alumina saturation index is considered to be a feature of the sedimentary source for granites (Antonelli et al., 2023; Wu et al., 2017). No correlation was observed between the $\delta^{122/118}\text{Sn}_{3161a}$ and A/CNK, Eu/Eu^* for S-type granites (Fig. S2). Therefore, plagioclase crystallization/accumulation and sediment addition play limited roles in affecting the Sn isotopic variability of S-type granites. The Ce/Pb ratio is regarded as an index of magma mixing (Jiang et al., 2022; Temizel, 2013). The $\delta^{122/118}\text{Sn}_{3161a}$ of LFB S-type granites in this study show no correlation with Ce/Pb (Table S1; Fig. S5a), ruling out the effect of magma mixing.

The S-type granites are derived from a more heterogeneous source region compared to I-type granites and represent the product of partial melting of deep-seated sedimentary rocks (Chappell and White, 1992). The A/CNK is higher for S-type granites with a sedimentary origin than I-type granites (Fig. S2a), and the average Sn content of S-type granites is higher than that of I-type granites (Chappell and White, 1992). The S-type granites from the Wagga Batholith located between 34.5 °S and 35.2 °S have lower $\delta^{122/118}\text{Sn}_{3161a}$ values than those from the southern and northern parts of the Wagga Batholith (Table S1). The possible explanation for the Sn isotope variations of S-type granites is source heterogeneity, as has been suggested for the Ba, K, and Cu isotope variations of S-type granites (Huang et al., 2020; Li et al., 2009; Nan et al., 2018). The relationship of $\delta^{122/118}\text{Sn}_{3161a}$ with $\text{Al}_2\text{O}_3 + \text{FeO} + \text{MgO} +$

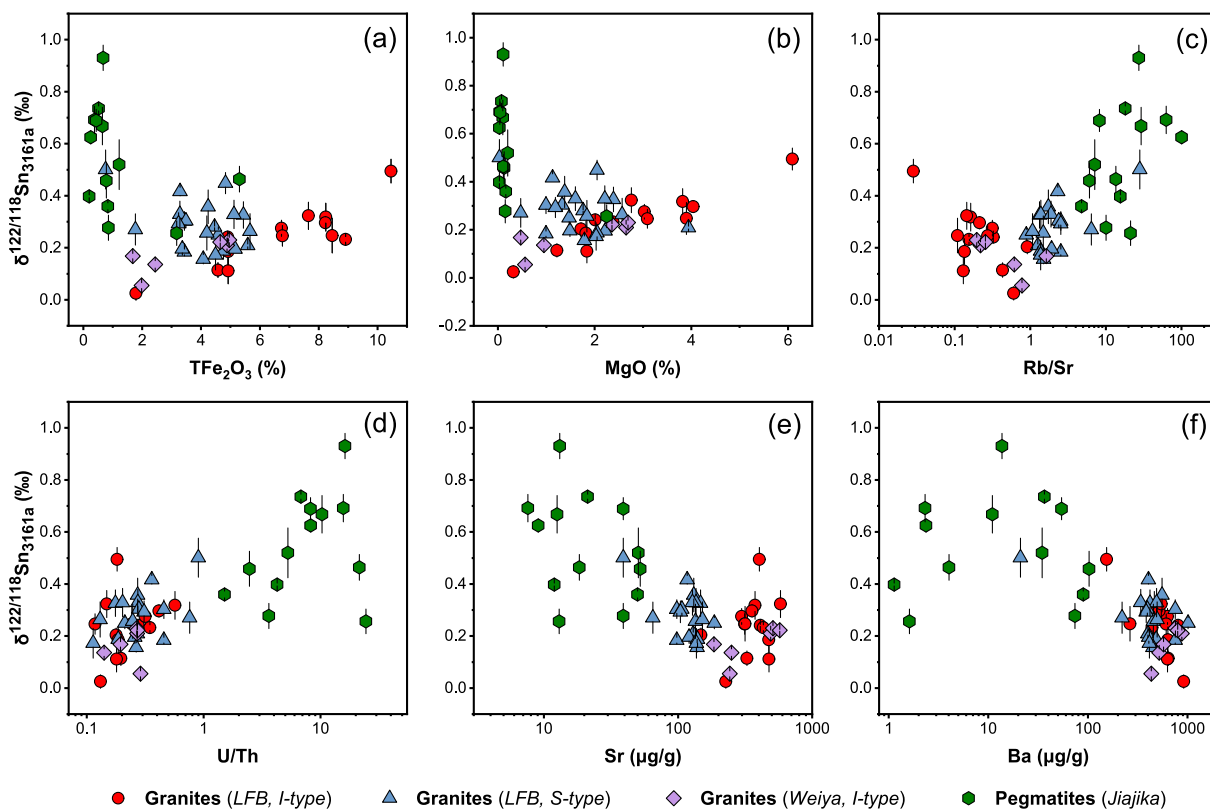


Fig. 5. Plots of $\delta^{122/118}\text{Sn}_{3161a}$ vs. TFe_2O_3 (wt%) (total Fe as Fe_2O_3) (a), MgO (wt%) (b), Rb/Sr (c), U/Th (d), Sr ($\mu\text{g/g}$) (e), and Ba ($\mu\text{g/g}$) (f) contents for granites and pegmatites investigated in this study.

Table 3

Tin isotopic compositions of pegmatites from borehole JSD-1 of Jiajika, China.

Sample	SiO_2 (wt%) ^a	TFe_2O_3 (wt%)	MgO (wt%)	TiO_2 (wt%)	Al_2O_3 (wt%)	Sn ($\mu\text{g g}^{-1}$)	$\delta^{122/118}\text{Sn}_{3161a}$ (‰)	2SD (‰)	N ^c
J027406b	74.35	0.65	0.10	0.02	14.71	21.39	0.668	0.072	4
J052615	74.10	0.83	0.16	0.06	14.26	10.45	0.360	0.013	3
J081910	73.66	0.78	0.13	0.02	15.01	17.11	0.458	0.067	3
J015412	73.06	0.85	0.15	0.06	14.73	17.18	0.277	0.048	3
J020618	74.61	0.52	0.07	0.02	13.96	7.99	0.736	0.009	3
J065530	76.25	0.67	0.11	0.02	12.15	6.22	0.930	0.049	3
J056204	73.28	0.38	0.04	0.00	14.93	5.08	0.692	0.053	4
J075032	69.85	5.30	0.11	0.01	13.98	9.24	0.464	0.050	4
J088312	76.04	1.21	0.20	0.04	12.08	10.76	0.520	0.096	3
J018012	71.73	0.44	0.05	0.01	16.39	4.24	0.689	0.043	4
J043706	78.47	0.20	0.03	0.00	12.65	6.97	0.398	0.005	3
Replicate ^b							0.350	0.056	
J070333	64.16	3.17	2.25	0.45	8.90	8.55	0.256	0.047	3
Replicate							0.249	0.064	3
J002306	74.95	0.25	0.03	0.00	15.16	63.77	0.625	0.023	3
Replicate							0.671	0.079	3

^a The major elements of data are from Luo et al. (2024).

^b Replicate in this table represents full procedural repeats, including sample dissolution, column chemistry, and instrumental measurement.

^c N in this table represents the number of repeat measurements in one session.

TiO_2 (wt.%) contents and $\text{Al}_2\text{O}_3/(\text{FeO} + \text{MgO} + \text{TiO}_2)$ ratios of granites from this study reveal that S-type granites exhibit a different source origin from I-type granites (Douce, 1999), despite their comparable $\delta^{122/118}\text{Sn}_{3161a}$ values (Fig. S4). When the sediments melt and form the S-type granitic magma, they may inherit the Sn isotope signature of the source materials.

5.1.3. Behavior of Sn isotopes in highly evolved magmatic systems

The Jiajika pegmatites display a significantly larger variability of Sn isotope compositions than the other UCC samples, including sediments (Table 3). One potential explanation is that pegmatites inherited the Sn

isotope signature of their sources, i.e., the metasedimentary rocks at Jiajika (Zhang et al., 2021). However, the available analyses of sediments (Fig. 2) reveal less variable and lower $\delta^{122/118}\text{Sn}_{3161a}$ values compared to pegmatites. The Jiajika granitic pegmatites have experienced extensive fractional crystallization (Zhang et al., 2021). However, the $\delta^{122/118}\text{Sn}_{3161a}$ values of the studied pegmatites show no obvious correlation with Rb/Sr , U/Th , K/Rb , or SiO_2 , the common proxies of magmatic differentiation (Table S1; Fig. 3, 5, S5). Therefore, the Sn isotope variability of the Jiajika pegmatites is unlikely to be caused by source inheritance or magmatic differentiation.

As shown in Fig. 6, the high $\delta^{122/118}\text{Sn}_{3161a}$ values of the Jiajika

Table 4

Tin isotopic compositions of loess and sediments investigated in this study.

Sample	SiO ₂ (wt%)	TFe ₂ O ₃ (wt%)	MgO (wt%)	TiO ₂ (wt%)	Al ₂ O ₃ (wt%)	Sn (μg g ⁻¹)	CIA ^c	δ ^{122/118} Sn _{3161a} (‰)	2SD (‰)	N ^d
Lingtai loess^a										
LT-25320	60.18	5.98	2.65	0.76	14.92	2.78	68.0	0.153	0.083	3
LT-21520	56.87	5.68	2.42	0.71	14.24	2.68	68.9	0.189	0.035	4
LT-16220	59.60	5.54	2.28	0.72	13.95	2.73	65.0	0.155	0.055	4
LT15600						2.69		0.239	0.020	4
LT14500						3.00		0.160	0.039	3
LT-14440	62.37	5.28	2.12	0.71	13.76	2.66	61.7	0.134	0.033	4
LT11600						3.07		0.132	0.034	4
LT-11460	55.97	4.76	1.80	0.64	12.30	2.37	61.9	0.175	0.033	4
LT11100						2.55		0.178	0.072	4
LT-10700	61.94	5.90	2.15	0.76	14.87	2.96	64.5	0.200	0.050	4
LT-9120	65.35	6.28	2.06	0.76	15.08	3.14	67.2	0.210	0.030	4
LT-8400	63.79	6.15	2.13	0.78	15.47	2.97	65.9	0.162	0.050	4
LT-8270	64.63	6.19	2.12	0.79	15.71	3.03	67.3	0.161	0.051	4
6810						3.30		0.233	0.072	4
LT6156						2.92		0.163	0.046	3
LT3650						2.90		0.163	0.033	4
LT-2700	64.34	5.99	2.10	0.78	15.17	3.01	65.9	0.182	0.030	4
LT-2410	64.22	5.71	2.32	0.76	14.73	2.88	61.9	0.182	0.051	4
LT-2130	64.28	5.90	2.07	0.76	15.11	2.96	65.6	0.160	0.075	4
LT-1236						2.31		0.211	0.043	4
East China Sea sediments										
S-1455						2.00		0.183	0.058	4
S-1465	56.71	5.32	2.46	0.68	12.82	2.84	57.3	0.327	0.014	4
S-1475	56.45	5.11	2.26	0.64	12.67	2.61	58.3	0.248	0.059	4
S-1477	68.33	4.28	1.60	0.72	9.96	3.15	51.9	0.311	0.061	4
S-1482	65.41	4.07	1.69	0.58	9.81	1.88	53.7	0.389	0.043	4
Zhe-Min rivers suspended sediments										
S-807						5.20		0.209	0.061	4
S-809						9.51		0.232	0.064	4
S-815						18.34		0.080	0.012	3
Duplicate ^b								0.040	0.042	4
S-823						5.54		0.195	0.056	4
Yangtze River sediments										
CJ22-1	61.11	5.16	1.85	0.700	12.55	3.14	64.7	0.208	0.082	3
CJ22-2	59.78	5.06	2.94	0.88	10.47	2.77	58.7	0.271	0.058	4
CJ22-5	52.16	6.92	2.86	0.73	16.59	3.21	70.0	0.191	0.034	4
CJ22-9	64.78	5.61	1.11	0.78	13.62	5.71	71.1	0.139	0.065	3
CJ22-12	61.58	5.94	2.06	0.91	13.28	4.09	67.9	0.156	0.032	4
D28	52.72	6.39	2.96	0.800	14.51	3.20	66.7	0.191	0.01	4
Duplicate								0.188	0.078	4
D07	76.89	1.75	0.68	0.28	5.01	1.07	54.4	0.308	0.051	3
D13	67.58	4.07	1.67	0.68	8.20	1.93	58.0	0.254	0.007	3
Duplicate								0.248	0.062	4
D08	73.73	1.88	0.83	0.27	5.00	1.02	54.7	0.490	0.019	4
Duplicate								0.501	0.048	4
Chaqiela shales										
DS2000	66.67	7.02	1.19	1.47	11.93	2.83	73.3	0.333	0.069	3
DS3000	66.30	6.54	1.06	1.46	11.50	2.91	69.2	0.351	0.027	3
Bohai Bay Clastic sedimentary rocks (Shahejie formation Sha3)										
B9	64.27	8.02	1.57	0.48	15.18	1.55	65.0	0.244	0.025	4
B49	64.39	5.05	1.43	0.87	16.60	1.96	70.1	0.217	0.053	4
B59	74.82	1.89	0.56	0.28	13.44	1.33	64.0	0.263	0.042	2
B61	67.30	4.07	1.25	0.47	14.34	1.37	66.0	0.192	0.058	3
B80	79.92	1.01	0.32	0.14	8.87	0.84	58.5	0.242	0.037	3

^a The Lingtai loess samples are from a single profile.^b Duplicate in this table represents repeat measurements on the same purified solution during different sessions.^c The chemical index of alteration (CIA) is defined as molar Al₂O₃/(Al₂O₃ + CaO* + Na₂O + K₂O), where CaO* refers to CaO in silicate (McLennan, 1993).^d N in this table represents the number of repeat measurements in one session.

pegmatites are generally accompanied by low Nb/Ta (<5) and high Rb/Th (>30) ratios, which are indicative of hydrothermal activity. Therefore, fluid activity is likely responsible for the highly variable and high δ^{122/118}Sn_{3161a} values in pegmatites. During the late-stage

crystallization of a granitic melt, Sn can be extracted by the exsolved fluid (Zhao et al., 2021). Based on the theoretical studies of Roskosz et al. (2020) and Wang et al., (2021a), the fluids would preferentially be enriched in lighter Sn isotopes relative to coexisting silicate melt. The

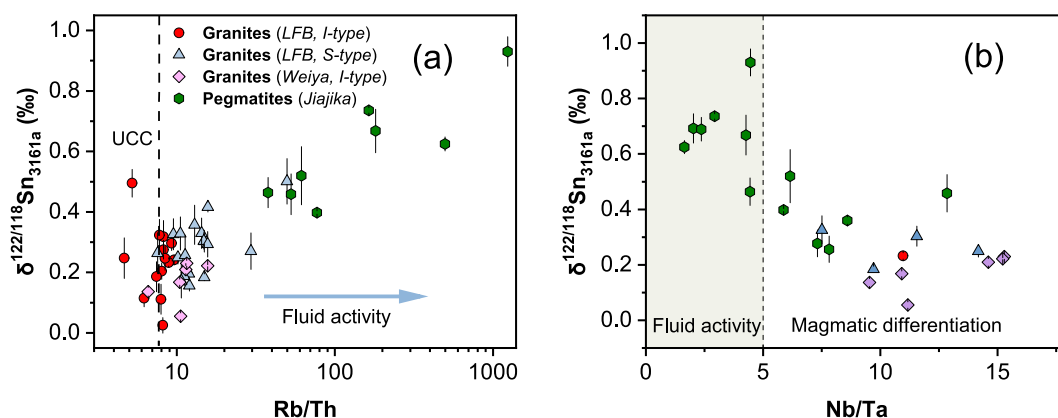


Fig. 6. Variations of $\delta^{122/118}\text{Sn}_{3161a}$ relative to (a) Rb/Th, (b) Nb/Ta for granites and pegmatites analyzed in this study. The Rb/Th ratio of the upper continental crust (UCC) is derived based on Rudnick and Gao, (2003) and samples with higher Rb/Th (indicated by the arrow in panel a) may be affected by fluids (Nan et al., 2018). The shaded area (Nb/Ta < 5) in panel b represents samples affected by fluids (Ballouard et al., 2016; Wu et al., 2017).

exsolution of fluid can thus leave the melt with isotopically heavier Sn, accounting for the observed Sn isotope signature of the pegmatites. The Laochang and Kafang granites from Gejiu also show significant Sn isotope variations (Fig. S6) that are comparable to Jiajika pegmatites investigated in this study (Sun et al., 2024). The Sn isotope variability of Gejiu granites can also be explained by the exsolution of an isotopically lighter fluid (Sun et al., 2024). Cassiterite has been occasionally observed in the JSD-1 borehole (Zhou et al., 2023), and cassiterite precipitated from the exsolved fluid could contain lighter Sn isotopes (Yao et al., 2018), complementary to the heavier Sn isotope compositions of pegmatites. It should be noted that the effect of crystal-melt separation cannot be fully excluded in a complex crystal-melt-fluid system. More theoretical and experimental work is therefore required to better constrain the Sn isotope fractionation between minerals and melts.

5.2. Tin isotope fractionation in surficial processes

5.2.1. Effect of chemical weathering

Understanding how various surficial processes can modify the Sn isotope compositions of sediments is critical for inferring the average Sn isotope composition of the upper continental crust. Loess typically samples a large area of exposed crust with limited chemical weathering and is regarded as a proxy for the average composition of UCC (Taylor et al., 1983). It was reported that Al, Ti, and Fe remain conservative while Ca, Sr, and Na are mobile during the chemical weathering of loess from the Chinese Loess Plateau (Gu et al., 1997; Jun et al., 1998). Tin is generally incorporated into minerals by substitution for Fe and Ti (Wang et al., 2013); thus, Sn should be immobile during loess formation. The CIA values of loess samples investigated in this study vary from 61.7 to 68.9 (Table S1), which may be considered as a moderate CIA range (Chen et al., 2016; Deng et al., 2022). The magnetic susceptibility of loess and paleosols represents a climate proxy for precipitation, vegetation, and, thus, monsoon intensity (An et al., 1991). The Lingtai loess samples display relatively limited Sn isotope variations with an average $\delta^{122/118}\text{Sn}_{3161a}$ of $0.177 \pm 0.059\text{‰}$ (2SD, $n = 20$). The $\delta^{122/118}\text{Sn}_{3161a}$ variations of loess display no correlation with depth (Table S1), magnetic susceptibility (Fig. S7), or CIA values (Table 4, S1). The narrow $\delta^{122/118}\text{Sn}_{3161a}$ range in loess thus appears to reflect the immobility of Sn and the predominance of mechanical weathering in loess formation.

Shales have also been used to reconstruct the composition of UCC (Condie, 1993). The formation of shales involves physical and chemical erosion, transportation, deposition, and diagenesis and is more complex compared to the formation of loess (Huang et al., 2020). In addition, it is difficult to place conclusive comparisons based on two shale samples since shales usually display larger isotopic variations (e.g. K, Mg

isotopes) than loess samples (Huang et al., 2020; Li et al., 2010). Two shale samples studied here display similar Sn isotope compositions with $\delta^{122/118}\text{Sn}_{3161a}$ of $0.333 \pm 0.069\text{‰}$ and $0.351 \pm 0.027\text{‰}$ (Fig. 7), which are isotopically heavier than those of loess samples.

As the CIA increases, the $\delta^{122/118}\text{Sn}_{3161a}$ values of clastic sedimentary rocks and modern sediments decrease (Fig. 7), and a negative correlation with diamicrites is established (Kubik et al., 2024). Specifically, the decrease of $\delta^{122/118}\text{Sn}_{3161a}$ for the Yangtze River sediments is associated with the increasing CIA and longitude (Fig. S8), demonstrating the progressively lighter Sn isotope compositions and more profound weathering downstream the Yangtze River. The weathering of Sn-bearing phases, such as biotite, titanite, sulfides, and Fe-Ti oxides, releases Sn into sediments (Anand and Gilkes, 1984; Peng et al., 2004). The released Sn can be adsorbed onto clay minerals and Fe-oxyhydroxides (Durce et al., 2022; Romer et al., 2022). The relationship between $\delta^{122/118}\text{Sn}_{3161a}$ and CIA can be ascribed to the preferential release of heavier Sn isotopes into aqueous solution or the incorporation

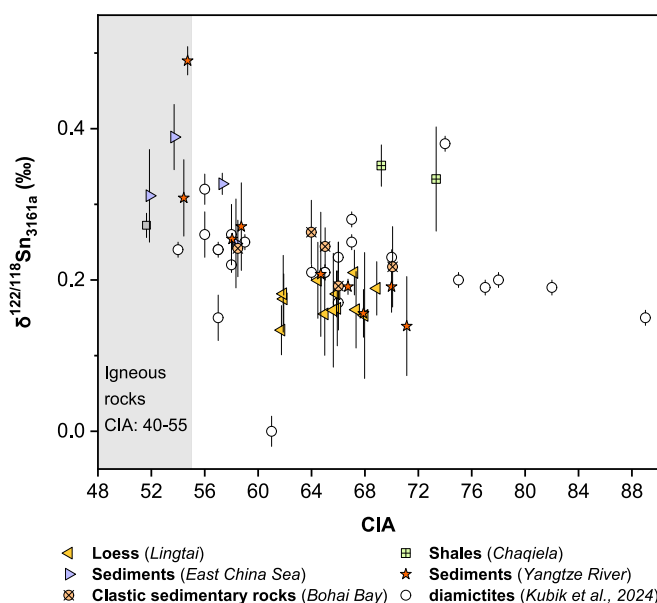


Fig. 7. The $\delta^{122/118}\text{Sn}_{3161a}$ compositions with respect to the chemical index of alteration (CIA) for sediments investigated in this study. The $\delta^{122/118}\text{Sn}_{3161a}$ of diamicrites are from Kubik et al. (2024). The chemical index of alteration (CIA) is defined as molar $\text{Al}_2\text{O}_3 / (\text{Al}_2\text{O}_3 + \text{CaO}^* + \text{Na}_2\text{O} + \text{K}_2\text{O})$, where CaO^* refers to CaO in silicate (McLennan, 1993). The shaded area represents fresh granites with CIA ranging from 45 to 55 (Nesbitt and Young, 1982).

of lighter Sn isotopes into secondary phases. In addition, Sn sulfides such as stannite usually host lighter Sn isotopes compared to oxides and silicate minerals (Sun et al., 2023; Wang et al., 2023; Yao et al., 2018). Tin released from sulfide weathering may enter the sediments, which can also explain the correlation between $\delta^{122/118}\text{Sn}_{3161a}$ and CIA. It should be noted that the sediments are composed of a mixture of weathering products and unweathered rock fragments (Guo et al., 2024). The declining trend of Sn isotope values with the increasing CIA of sediments could also originate from sampling bias. Further insights from silicate weathering profiles are needed to constrain Sn elemental and isotopic behavior during chemical weathering.

5.2.2. Effect of sorting and provenance

The removal of minerals due to hydrodynamic sorting can affect the elemental and isotopic compositions of sediments. Al_2O_3 and Fe_2O_3 are enriched in fine-grained fractions since phyllosilicates are rich in Al and Fe, while Na_2O , SiO_2 , and Hf are mostly hosted in plagioclase, quartz, and zircon, respectively (Sauzéat et al., 2015). As the intensity of chemical weathering increases, clay fractions dominate over primary minerals in sediments, accompanied by the increase of Al_2O_3 and Fe_2O_3 and a decrease of SiO_2 , Na_2O , K_2O , and CaO in sediments (Tian et al., 2021). The Al/Ti and Al/Zr ratios, which reflect the relative proportions of Al-rich clay phases versus Fe-Ti oxides or Zr-rich dense minerals (Aarons et al., 2023), can be used as a proxy for the mineral sorting effect. The lack of correlation between $\delta^{122/118}\text{Sn}_{3161a}$ with the above ratios (Fig. 8a, b) indicates that sorting may not be the primary control of the Sn isotope composition of the sediments.

The provenance difference may account for the Sn isotope heterogeneity of modern sediments and sedimentary rocks. The samples collected here were from different locations with mixed lithologies and had variable chemical compositions, implying differences among the source rock components. This can be evaluated using elemental proxies not significantly affected by sedimentary processes, such as the ratio of insoluble elements Th/Sc that trace the contributions of felsic and mafic materials (Bi et al., 2017). Scandium is generally more compatible than Th during magma differentiation and tends to be enriched in mafic igneous rocks, while Th is enriched in the residual melt (Bi et al., 2017). The mafic end members have low Th/Sc ratios (0.078 on average for basalts from EarthChem Portal) with reported $\delta^{122/118}\text{Sn}_{3161a}$ of mafic rocks ranging from -0.520‰ to 0.540‰ (Badullovich et al., 2017; She et al., 2023a; Wang et al., 2018). The felsic end members have high Th/Sc ratios (4.023 on average for granites from EarthChem Portal) with $\delta^{122/118}\text{Sn}_{3161a}$ of felsic rock spanning from 0.025‰ to 0.933‰ (She et al., 2023b; Sun et al., 2024; Wang et al., 2022b). The Sn isotope

compositions of these two endmembers span a large range (Fig. 8c) and need further scrutiny via future targeted studies. The data currently available is yet insufficient to determine whether the Sn isotope variations of sediments are solely caused by mixing.

5.3. The average Sn isotope composition of the upper continental crust

The average Sn isotopic composition of UCC can serve as a baseline for assessing how Sn isotopes can be fractionated during its cycling on Earth's surface. Generally, the composition of the upper continental crust can be estimated by two approaches, including a weighted average of samples exposed at the surface and fine-grained clastic sedimentary rocks (Hu et al., 2022; Huang et al., 2020; Nan et al., 2018) or Aeolian/glacial deposits (Li et al., 2023; Mazza et al., 2024; Rudnick and Gao, 2014). Both methods are used here to characterize the Sn isotope composition of UCC.

The difficulty in estimating the average $\delta^{122/118}\text{Sn}_{3161a}$ of UCC lies in estimating the proportion of major rock types comprising UCC, the corresponding Sn contents, and the respective $\delta^{122/118}\text{Sn}_{3161a}$ values. Wedepohl (1995) suggested that upper crustal rocks can be divided into six major rock units (Table 5): 14% sediments, 25% granites, 20% granodiorites, 5% tonalites, 6% gabbros, and 30% metamorphic rocks. The average Sn contents in these rock units can be estimated using the chemical compositions of different rock units included in the EarthChem Portal and GEOROC databases (Table 5). We adopted the Monte-Carlo approach (Wu et al., 2022) to estimate the average of Sn contents in each rock unit. One hundred data was randomly selected to calculate an average value, and this process was repeated 1000 times to derive a mean value. Using this approach, the average Sn concentration for UCC was estimated to be $4.46 \pm 0.93 \mu\text{g/g}$ (Table 5), which is slightly above the average of previous estimations ($1.73\text{--}5.5 \mu\text{g/g}$, with an average of $3.07 \pm 3.33 \mu\text{g/g}$) (Gaschnig et al., 2016; Rudnick and Gao, 2003). It should be noted that Sn is a volatile trace element that resides in refractory minerals (cassiterite, rutile); thus, it should be cautioned that Sn concentration data from the literature may be of variable quality. Nonetheless, because the proportions, rather than absolute masses, matter in estimating the average $\delta^{122/118}\text{Sn}_{3161a}$ of UCC, random inaccuracy in the Sn content of rocks from the database is not expected to introduce significant errors to the average $\delta^{122/118}\text{Sn}_{3161a}$ of UCC.

The $\delta^{122/118}\text{Sn}_{3161a}$ values of different geological samples from this study are used to derive the Sn isotope composition of UCC (Table 5). S-type granite sample VB21 has the lowest K/Rb and the highest Rb/Sr and $\delta^{122/118}\text{Sn}_{3161a}$ value among the LFB S-type granites (Table 2; Fig. 5, S1e, f). The sample VB21 and Jiajika pegmatites have experienced

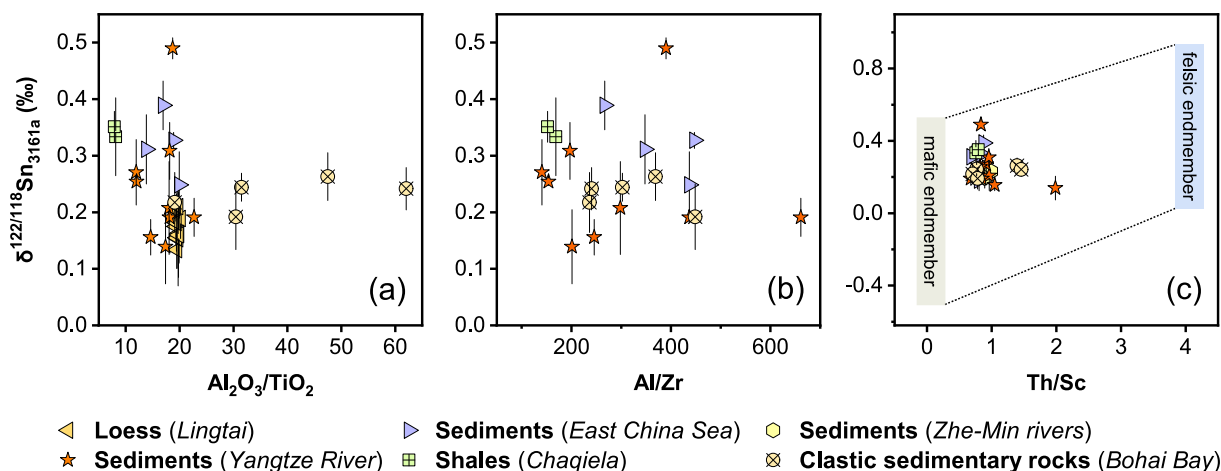


Fig. 8. $\delta^{122/118}\text{Sn}_{3161a}$ vs. (a) $\text{Al}_2\text{O}_3/\text{TiO}_2$, (b) Al/Zr , (c) Th/Sc for sediments analyzed in this study, the dotted lines in panel c indicate the mixing lines of a felsic endmember ($\text{Th}/\text{Sc} = 4.023$, $\delta^{122/118}\text{Sn}_{3161a} = 0.025$ to 0.930‰) (She et al., 2023b; Sun et al., 2024; Wang et al., 2022b) and a mafic endmember ($\text{Th}/\text{Sc} = 0.078$, $\delta^{122/118}\text{Sn}_{3161a} = -0.520$ to 0.540‰) (Badullovich et al., 2017; She et al., 2023a; Wang et al., 2018).

Table 5
Mass balance model for Sn content and isotope composition of the upper continental crust (UCC).

Method	Rock units ^a	Proportions in UCC (%) ^a	Average Sn contents (μg/g) ^b	Fraction of Sn in UCC (%) ^c	Average $\delta^{122/118}\text{Sn}_{3161a}$ (‰) ^d	2SD (‰)
	Sediments	14	6.17 ± 0.52	20.48	0.217	0.152
	Granites	25	4.17 ± 0.35	24.72	0.245	0.191
	Granodiorites	20	1.92 ± 0.15	9.11	0.245	0.191
	Tonalites ^e	5	1.40 ± 0.10			
	Gabbros ^e	6	2.86 ± 0.32			
	Metamorphic rocks	30	6.42 ± 0.59	45.68	0.231	0.173
Lithology-average ^f	UCC		4.46 ± 0.93	100.00	0.233	0.099
Loess average ^g	UCC		2.85 ± 0.50		0.177	0.059
Empirical igneous array	UCC		2.86 ± 2.40 ^h		0.197	0.153 ^h

^a Division of the rock units and respective proportion in the upper continental crust are from Wedepohl (1995).
^b The average Sn contents of sediments, granites, granodiorites, tonalites, gabbros, and metamorphic rocks are derived from EarthChem Portal and GEOROC databases.
^c The proportion of Sn in UCC is calculated based on the proportion of rock units and average Sn contents for each rock unit.
^d The average $\delta^{122/118}\text{Sn}_{3161a}$ and 2SD of sediments, granites, and granodiorites are based on samples analyzed here. The average $\delta^{122/118}\text{Sn}_{3161a}$ and 2SD of metamorphic rocks are based on the results of granites here by assuming no Sn isotope fractionation during metamorphism.
^e The gabbro and tonalite are not included in the final mass balance calculation because their Sn isotope compositions remain undetermined, and these two rock units account for only a small Sn budget.
^f The lithology-average $\delta^{122/118}\text{Sn}_{3161a}$ and 2SD of the upper continental crust is derived from the following equations: weighted average = $\Sigma(\delta^{122/118}\text{Sn} \times \text{Sn proportion})$, 2SD of weighted average = $\sqrt{(\Sigma(2\text{SDrock unit} \times \text{Sn proportion})^2)}$, where Sn proportion is the proportion of Sn in each rock unit in the upper continental crust.
^g The “loess average” method is based on the average Sn contents and isotope compositions of loess from this study.
^h The “empirical igneous array” method is based on the trend lines between $\delta^{122/118}\text{Sn}$, Sn contents, and SiO₂ contents of I-type granites. The cross of SiO₂ contents of UCC (66.6%) and these trend lines are the regression results, which are indicated by stars in Fig. 8b and Fig. S4b.

strong fractional crystallization or fluid activity. Thus, they are excluded when calculating the average UCC composition. To estimate the average Sn isotope composition of UCC, we first derived an average $\delta^{122/118}\text{Sn}_{3161a}$ value of $0.245 \pm 0.191\text{‰}$ (n = 41, 2SD) for the “granite” and “granodiorites” endmembers. Then, the average values of modern sediments, loess, shales, and clastic sedimentary rocks were calculated, which yielded an average $\delta^{122/118}\text{Sn}_{3161a}$ value of $0.217 \pm 0.152\text{‰}$ (n = 45, 2SD) for the “sediments” endmember. The “tonalites” and “gabbros” endmembers are neglected here as data for these rock types are lacking and they account for only 2.95% of the Sn budget of UCC. The Sn isotopic compositions of metamorphic rocks remain unconstrained. We

assume that Sn isotopes do not fractionate during metamorphism and use the average Sn isotope compositions of granites and sediments ($0.231 \pm 0.173\text{‰}$) from this study to represent the bulk average of all “metamorphic rocks” following the previous study of Wu et al. (2022). Therefore, the lithology-weighted $\delta^{122/118}\text{Sn}_{3161a}$ of UCC is estimated to be $0.233 \pm 0.099\text{‰}$. We note that the lithology-weighted average Sn isotope composition of the UCC could be further refined with updated data of metamorphic rocks, tonalites, and gabbros in future studies.

In addition, the I-type granites define an empirical igneous array on a plot of $\delta^{122/118}\text{Sn}_{3161a}$ versus SiO₂ (Fig. 9b). Using this igneous array and the average upper crustal contents of SiO₂ (66.6%) (Rudnick and Gao,

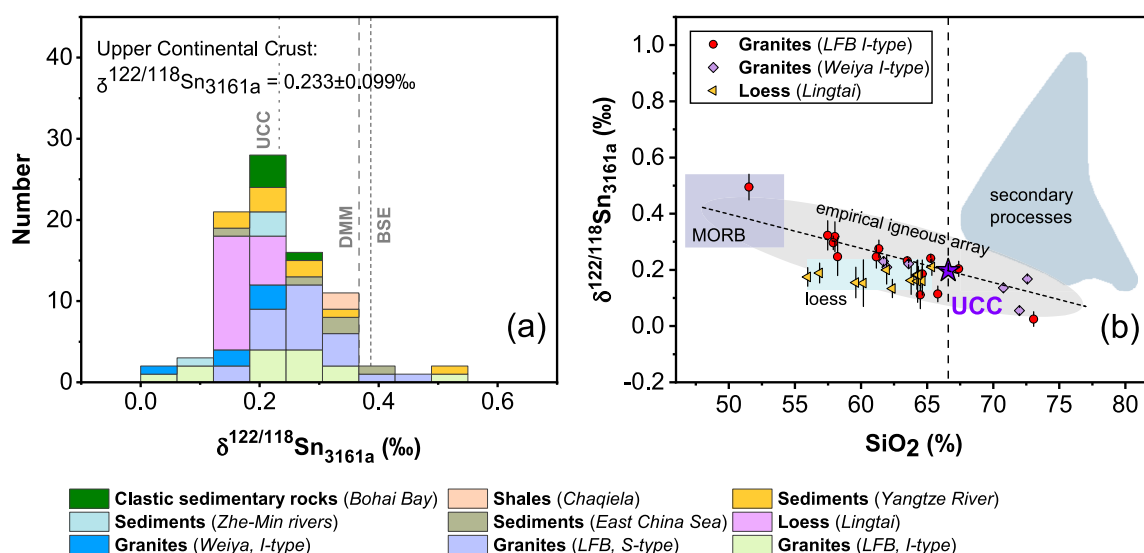


Fig. 9. (a) Histogram of $\delta^{122/118}\text{Sn}_{3161a}$ values for UCC samples analyzed in this study. The recommended average Sn isotopic composition for the upper continental crust (UCC) is $0.233 \pm 0.099\text{‰}$ (2SD) (Table 5). (b) $\delta^{122/118}\text{Sn}_{3161a}$ versus SiO₂ (wt%) contents for I-type granites and loess from this study. The $\delta^{122/118}\text{Sn}_{3161a}$ for the MORB (purple rectangle), depleted MORB mantle (DMM) (dashed line in panel a), and bulk silicate Earth (BSE) (short dashed line in panel a) are from She et al., (2023a) and Badullovich et al. (2017). The purple star indicates the derived Sn isotope composition of UCC based on the empirical igneous array and SiO₂ (wt%) content from Rudnick and Gao (2003).

2003), the $\delta^{122/118}\text{Sn}_{3161a}$ value of $0.197 \pm 0.153\text{‰}$ (2SD) for UCC can be interpolated (Fig. 9b). This value is consistent with the average $\delta^{122/118}\text{Sn}_{3161a}$ of loess ($\delta^{122/118}\text{Sn}_{3161a} = 0.177 \pm 0.059\text{‰}$, 2SD). An average Sn content ($2.86 \pm 2.40 \mu\text{g/g}$) can be derived in a similar fashion based on an empirical igneous array of Sn content versus SiO_2 (Fig. S3b). This estimation aligns well with the loess average ($2.85 \pm 0.50 \mu\text{g/g}$), and the average estimate of previous studies on the Sn concentration of UCC ($3.07 \pm 3.33 \mu\text{g/g}$) (Gaschnig et al., 2016; Rudnick and Gao, 2003), which supports the validity of “empirical igneous array” approach for estimating the average $\delta^{122/118}\text{Sn}_{3161a}$. The lithology-weighted average Sn isotope composition ($0.233 \pm 0.099\text{‰}$) is consistent with results from the “loess average” and “empirical igneous array” methods and is considered to be the best estimate of the average Sn isotopic composition of UCC (Fig. 9a). It should be noted that our estimates align closely with the new measurements of diamictites ($\delta^{122/118}\text{Sn}_{3161a} = 0.220 \pm 0.140\text{‰}$) (Kubik et al., 2024). Considering the growing but still insufficient Sn isotope dataset, our estimates for UCC should be taken as a preliminary Sn isotopic baseline for UCC.

5.4. Implications of the Sn isotope compositions of the upper crust

Previous studies have constrained the average Sn isotope compositions of the depleted mantle ($\delta^{122/118}\text{Sn}_{3161a} = 0.367\text{‰}$) (She et al., 2023a) and primitive mantle ($\delta^{122/118}\text{Sn}_{3161a} = 0.387\text{‰}$) (Badullovich et al., 2017). The upper continental crust, despite its significant Sn isotopic heterogeneity, is on average isotopically lighter by $\sim 0.13\text{‰}$ to $\sim 0.15\text{‰}$ than the mantle (Fig. 9a). Considering that Sn is significantly enriched in the crust ($\sim 1.7 \mu\text{g/g}$ in the bulk crust) compared to the mantle ($0.12\text{--}0.17 \mu\text{g/g}$ in the primitive mantle) (Rudnick and Gao, 2003; She et al., 2023a), the Sn isotopic difference between UCC and mantle indicates significant elemental and isotopic fractionation of Sn during Earth’s differentiation and crustal evolution.

The difference in the Sn isotope composition between UCC and mantle may originate from the mantle-crust differentiation process. Tin is incompatible during partial melting, resulting in the enrichment of Sn in the melt (Jochum et al., 1993; Wang et al., 2018). This is manifested by higher Sn content of basalts ($0.53\text{--}5.75 \mu\text{g/g}$) relative to peridotites ($0.13\text{--}0.21 \mu\text{g/g}$) and komatiites ($0.15\text{--}0.36 \mu\text{g/g}$) (Badullovich et al., 2017; She et al., 2023a; Wang et al., 2018). However, partial melting tends to enrich the melt in heavier Sn isotopes (Wang et al., 2018), which is opposite to the observation that UCC is isotopically lighter than the mantle. Thus, partial melting of the mantle alone cannot account for the lower $\delta^{122/118}\text{Sn}_{3161a}$ of UCC. Intracrustal magmatic differentiation of Fe-Ti oxides may be one potential explanation. As shown in Fig. S9a, b, the $\delta^{122/118}\text{Sn}$ values of I-type granites, basalts, and komatiites decrease with decreasing bulk-rock MgO contents, while, at the same time, Sn abundance increases. This observation leads us to propose that the accumulation and subsequent transfer of Fe-Ti oxides from the lower crust into the mantle (Ducea et al., 2021; Frost and Shive, 1986; Liu et al., 2023; Zieman et al., 2024) is responsible for the low $\delta^{122/118}\text{Sn}$ of evolved upper continental crust (Rudnick, 1995; Rudnick and Gao, 2003). This hypothesis is supported by the accumulation of Fe-Ti oxides in lower crustal rocks (Liu et al., 2023; Liu et al., 2024; Stepanov et al., 2024; Zhang et al., 2020), as well as the concurrent decrease in $\delta^{122/118}\text{Sn}$ and compositional shift from basaltic to andesitic in the Kilauea Iki (KI) lava lake, attributed to Fe-Ti oxide crystallization (Badullovich et al., 2017; Teng et al., 2008). Therefore, the fractionation of Fe-Ti oxides during intracrustal differentiation can explain the relatively low $\delta^{122/118}\text{Sn}$ in the andesitic UCC compared to the mantle.

The subduction zones are the essential places for exchanging mantle and crustal materials (Hao et al., 2024; Stern, 2002), and the formation of Sn ore deposits is closely related to subduction zones (Sun et al., 2012). Both crustal and mantle materials are involved in forming Sn-bearing granites and Sn deposits (Chen et al., 2013; Kunz et al., 2022). The Sn isotopic difference between crust and mantle enables Sn isotopes to be a potential tool for tracing the source and contribution of Sn ore-

forming materials and subduction-related rocks. Additionally, source enrichment and fractional crystallization have been proposed to play critical roles in forming Sn ore deposits (Lehmann, 2021; Romer and Kroner, 2015), and hydrothermal fluids can sequester large amounts of Sn to form Sn deposits (Zhao et al., 2021). Fluids with highly variable $\delta^{122/118}\text{Sn}_{3161a}$ exsolved from upper crustal melts can favor the transport and enrichment of Sn, as suggested by a Sn isotope study on Gejiu granites (Sun et al., 2024). Therefore, Sn isotope signatures may be utilized to probe fluid processes and the enrichment and mineralization of Sn. A compilation of published Sn isotope data (Berger et al., 2018; Berger et al., 2019; Brugmann et al., 2017; Mason et al., 2020; Mason et al., 2016; Mathur et al., 2024; Powell et al., 2022; She et al., 2023c; Wang et al., 2019a; Wu et al., 2023; Yao et al., 2018) suggests that Sn in hydrothermal cassiterites is overall isotopically heavier than UCC (Fig. 10), although current database of Sn isotope compositions of cassiterite displays a notable range. However, according to first-principles calculations, heavier Sn isotopes preferentially partition into silicates compared to cassiterite under equilibrium (Wang et al., 2023). This contrast implies that cassiterite in hydrothermal deposits is not a product of magmatic crystallization but hydrothermal precipitation. Strong isotope fractionation of Sn must have therefore occurred during the magmatic-hydrothermal stages involving hydrothermal fluids.

6. Concluding remarks

The following main conclusions can be drawn from the high-precision Sn isotopic analyses of a suit of 100 continental crustal rocks:

- (1) Significant $\delta^{122/118}\text{Sn}_{3161a}$ variations for I-type ($0.025 \pm 0.026\text{‰}$ to $0.495 \pm 0.046\text{‰}$) and S-type ($0.156 \pm 0.018\text{‰}$ to $0.501 \pm 0.075\text{‰}$) granites from the Lachlan Fold Belt, Australia, and Central Asian Orogenic Belt, China can be linked to fractional crystallization of Fe-bearing minerals and source heterogeneity.
- (2) The Jiajika pegmatites show relatively large $\delta^{122/118}\text{Sn}_{3161a}$ variations, varying from $0.256 \pm 0.047\text{‰}$ to $0.930 \pm 0.049\text{‰}$. This

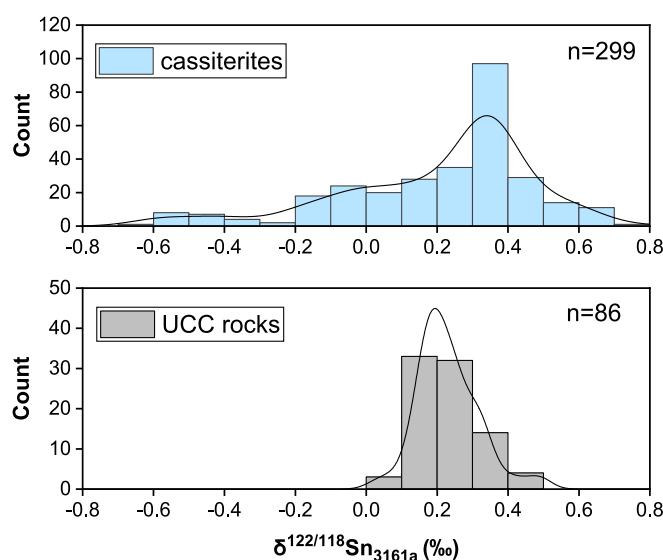


Fig. 10. Histogram of $\delta^{122/118}\text{Sn}_{3161a}$ values of cassiterite from literature (Berger et al., 2018; Berger et al., 2019; Brugmann et al., 2017; Mason et al., 2020; Mason et al., 2016; Mathur et al., 2024; Powell et al., 2022; She et al., 2023c; Wang et al., 2019; Wu et al., 2023; Yao et al., 2018) and upper continental crust rocks (pegmatite excluded) investigated in this study. The Sn isotope data from the literature were converted to $\delta^{122/118}\text{Sn}_{3161a}$ using kinetic fractionation law (Young et al., 2002) and referencing the standard solutions from Brugmann et al., 2017.

heavier Sn isotopic composition of pegmatites compared to the average UCC likely reflects the involvement of fluids.

- (3) Loess samples have relatively invariant $\delta^{122/118}\text{Sn}_{3161a}$ values with an average of $0.177 \pm 0.059\%$. The $\delta^{122/118}\text{Sn}_{3161a}$ values of sediments can be related to chemical weathering or mixing of felsic and mafic rocks.
- (4) Overall, the upper continental crust has a heterogeneous Sn isotopic composition, ranging from $0.025 \pm 0.026\%$ to $0.930 \pm 0.049\%$, with a lithology-weighted average $\delta^{122/118}\text{Sn}_{3161a}$ of $0.233 \pm 0.099\%$. Tin in UCC is isotopically lighter than the mantle by $\sim 0.13\%$ to $\sim 0.15\%$ in $\delta^{122/118}\text{Sn}_{3161a}$, underlining significant elemental and isotopic fractionation of Sn during Earth's differentiation and crustal evolution.

Data availability

Data are available through Mendeley Data at <https://doi.org/10.17632/txy8v3679s.1>.

CRediT authorship contribution statement

Jia-Xin She: Writing – review & editing, Writing – original draft, Visualization, Validation, Methodology, Investigation, Formal analysis, Data curation. **Weiqiang Li:** Writing – review & editing, Writing – original draft, Supervision, Resources, Investigation, Funding acquisition, Formal analysis, Conceptualization. **Edith Kubik:** Writing – review & editing, Investigation. **Frédéric Moynier:** Writing – review & editing, Supervision, Resources. **Xiang-Long Luo:** Methodology, Investigation. **Jun Mu:** Methodology, Investigation. **Shichao An:** Methodology, Investigation. **Chang-Zhi Wu:** Validation, Resources. **Zhongya Hu:** Resources, Investigation. **Junfeng Ji:** Validation, Resources.

Declaration of competing interest

The authors declare that they have no known competing financial interests or personal relationships that could have appeared to influence the work reported in this paper.

Acknowledgment

Constructive suggestions from Ryan Mathur and two anonymous reviewers, associated editor Tomas Magna, and editorial handling of Jeffrey G. Catalano greatly improved this manuscript. We thank Zhiqin Xu, A. I. S. Kemp, Yongxiang Li, Xia Zhang, Xinyu Liu, and Shuya Huang for their help with the samples. This study was supported by Frontiers Science Center for Critical Earth Material Cycling, Nanjing University (Grant Number: DLTD2103), China National Space Administration (Grant Number: D020205), and National Natural Science Foundation of China (Grant Number: 41873004) to WL.

Appendix A. Supplementary material

The Supplementary materials contain (1) Supplementary material 1 – Table S1 summarizes the data range for all the investigated samples and detailed elemental and isotopic compositions for the samples from this study. (2) Supplementary material 2 – Fig. S1 describes the detailed elemental compositions for granites and pegmatites. Fig. S2 is the relationship of $\delta^{122/118}\text{Sn}_{3161a}$ and A/CNK or Eu/Eu*. Fig. S3 plots the elemental compositions for I-type granites. Fig. S4 shows the relationship of $\delta^{122/118}\text{Sn}_{3161a}$ with $\text{Al}_2\text{O}_3 + \text{FeO} + \text{MgO} + \text{TiO}_2$ (wt.%) contents and $\text{Al}_2\text{O}_3/(\text{FeO} + \text{MgO} + \text{TiO}_2)$ ratios for granites from this study. Fig. S5 plots $\delta^{122/118}\text{Sn}_{3161a}$ with Ce/Pb or K/Rb ratios for S-type granites and pegmatites. Fig. S6 is $\delta^{122/118}\text{Sn}_{3161a}$ of Laochang and Kafang granites compared with granites and pegmatites from this study. Fig. S7 shows the loess's Sn isotope composition versus age and magnetic susceptibility. Fig. S8 is the CIA and $\delta^{122/118}\text{Sn}_{3161a}$ with the

longitude of Yangtze River sediments. Fig. S9 shows the relationship between $\delta^{122/118}\text{Sn}_{3161a}$ or Sn contents with MgO contents of I-type granites from this study compared with OIBs, Komatiites, and MORBs from the literature. Table S2 compares the instrumental operation parameters for Sn isotopic analysis at Nanjing University and IPGP. Supplementary material to this article can be found online at <https://doi.org/10.1016/j.gca.2024.07.029>.

References

- Aarons, S.M., Dauphas, N., Greber, N.D., Roskosz, M., Bouchez, J., Carley, T., Liu, X.-M., Rudnick, R.L., Gaillardet, J., 2023. Titanium transport and isotopic fractionation in the Critical Zone. *Geochim. Cosmochim. Acta* 352, 175–193.
- Adam, J., Green, T., 2006. Trace element partitioning between mica- and amphibole-bearing garnet lherzolite and hydrous basanitic melt: 1. Experimental results and the investigation of controls on partitioning behaviour. *Contrib. Mineral. Petrol.* 152, 1–17.
- An, Z., Kukla, G.J., Porter, S.C., Xiao, J., 1991. Magnetic susceptibility evidence of monsoon variation on the Loess Plateau of central China during the last 130,000 years. *Quat. Res.* 36, 29–36.
- Anand, R.R., Gilkes, R.J., 1984. Weathering of ilmenite in a lateritic pallid zone. *Clay Clay Miner.* 32, 363–374.
- Antonelli, M.A., Yakymchuk, C., Schauble, E.A., Foden, J., Janoušek, V., Moyen, J.-F., Hoffmann, J., Moynier, F., Bachmann, O., 2023. Granite petrogenesis and the $\delta^{84}\text{Ca}$ of continental crust. *Earth Planet. Sci. Lett.* 608, 118080.
- Badullovich, N., Moynier, F., Creech, J., Teng, F.Z., Sossi, P.A., 2017. Tin isotopic fractionation during igneous differentiation and Earth's mantle composition. *Geochem. Perspect. Lett.* 5, 24–28.
- Bali, E., Audéat, A., Keppler, H., 2011. The mobility of U and Th in subduction zone fluids: an indicator of oxygen fugacity and fluid salinity. *Contrib. Mineral. Petrol.* 161, 597–613.
- Ballouard, C., Poujol, M., Boulvais, P., Branquet, Y., Tartèse, R., Vigneresse, J.-L., 2016. Nb-Ta fractionation in peraluminous granites: A marker of the magmatic-hydrothermal transition. *Geology* 44, 231–234.
- Balsam, W., Ji, J., Chen, J., 2004. Climatic interpretation of the Luochuan and Lingtai loess sections, China, based on changing iron oxide mineralogy and magnetic susceptibility. *Earth Planet. Sci. Lett.* 223, 335–348.
- Bau, M., 1996. Controls on the fractionation of isoivalent trace elements in magmatic and aqueous systems: evidence from Y/Ho, Zr/Hf, and lanthanide tetrad effect. *Contrib. Mineral. Petrol.* 123, 323–333.
- Bea, F., Pereira, M.D., Stroth, A., 1994. Mineral/leucosome trace-element partitioning in a peraluminous migmatite (a laser ablation-ICP-MS study). *Chem. Geol.* 117, 291–312.
- Berger, D., Figueiredo, E., Bruegmann, G., Pernicka, E., 2018. Tin isotope fractionation during experimental cassiterite smelting and its implication for tracing the tin sources of prehistoric metal artefacts. *J. Archaeol. Sci.* 92, 73–86.
- Berger, D., Soles, J.S., Giunlià-Mair, A.R., Brüggmann, G., Galili, E., Lockhoff, N., Pernicka, E., 2019. Isotope systematics and chemical composition of tin ingots from Mochlos (Crete) and other Late Bronze Age sites in the eastern Mediterranean Sea: An ultimate key to tin provenance? *PLoS One* 14, e0218326.
- Bi, L., Yang, S., Zhao, Y., Wang, Z., Dou, Y., Li, C., Zheng, H., 2017. Provenance study of the Holocene sediments in the Changjiang (Yangtze River) estuary and inner shelf of the East China sea. *Quat. Int.* 441, 147–161.
- Brown, M., 2013. Granite: From genesis to emplacement. *Geol. Soc. Am. Bull.* 125, 1079–1113.
- Brugmann, G., Berger, D., Pernicka, E., 2017. Determination of the Tin Stable Isotopic Composition in Tin-bearing Metals and Minerals by MC-ICP-MS. *Geostand. Geoanal. Res.* 41, 437–448.
- Chappell, B.W., White, A.J.R., 1992. I- and S-type granites in the Lachlan Fold Belt. *Earth Environ. Sci. Trans. R. Soc. Edinb.* 83, 1–26.
- Chen, Z., Ding, Z., Yang, S., Zhang, C., Wang, X., 2016. Increased precipitation and weathering across the Paleocene-Eocene Thermal Maximum in central China. *Geochem., Geophys. Geosyst.* 17, 2286–2297.
- Chen, X., Qu, X., Xu, S., Wang, W., Li, S., He, H., Liu, Y., 2020. Dissolution pores in shale and their influence on reservoir quality in Damintun Depression, Bohai Bay Basin, East China: insights from SEM images, N₂ adsorption and fluid-rock interaction experiments. *Mar. Pet. Geol.* 117, 104394.
- Chen, J., Wang, R., Zhu, J., Lu, J., Ma, D., 2013. Multiple-aged granitoids and related tungsten-tin mineralization in the Nanling Range, South China. *Sci. China Earth* 56, 2045–2055.
- Chen, S.-C., Yu, J.-J., Bi, M.-F., Lehmann, B., 2022. Tin-bearing minerals at the Furong tin deposit, South China: Implications for tin mineralization. *Geochem.* 82, 125856.
- Condie, K.C., 1993. Chemical composition and evolution of the upper continental crust: Contrasting results from surface samples and shales. *Chem. Geol.* 104, 1–37.
- Creech, J.B., Moynier, F., 2019. Tin and zinc stable isotope characterisation of chondrites and implications for early Solar System evolution. *Chem. Geol.* 511, 81–90.
- Creech, J.B., Moynier, F., Badullovich, N., 2017. Tin stable isotope analysis of geological materials by double-spike MC-ICPMS. *Chem. Geol.* 457, 61–67.
- Da, J., Brecker, D.O., Li, T., Li, G., Lu, H., Ji, J., 2023. A humid East Asia during the Early Pliocene Indicated by Calcite Nodules From the Chinese Loess Plateau. *Paleoceanogr. Paleoclimatol.* 38, e2023PA004615.
- Deng, K., Yang, S., Guo, Y., 2022. A global temperature control of silicate weathering intensity. *Nat. Commun.* 13, 1781.

- Ding, Z.L., Xiong, S.F., Sun, J.M., Yang, S.L., Gu, Z.Y., Liu, T.S., 1999. Pedostratigraphy and paleomagnetism of a ~7.0 Ma eolian loess–red clay sequence at Lingtai, Loess Plateau, north-central China and the implications for paleomonsoon evolution. *Palaeogeogr. Palaeoclimatol.* 152, 49–66.
- Douce, A.E.P., 1999. What do experiments tell us about the relative contributions of crust and mantle to the origin of granitic magmas?, in: Castro, A., Fernández, C., Vigneresse, J.L. (Eds.), *Understanding Granites: Integrating New and Classical Techniques*. Geological Society of London, pp. 55–75.
- Duan, Z.-P., Jiang, S.-Y., Su, H.-M., Zhu, X.-Y., Zou, T., Cheng, X.-Y., 2021. Geochronological and geochemical investigations of the granites from the giant Shihuiyao Rb-(Nb-Ta-Be-Li) deposit, Inner Mongolia: implications for magma source, magmatic evolution, and rare metal mineralization. *Lithos* 400–401, 106415.
- Ducea, M.N., Chapman, A.D., Bowman, E., Triantafyllou, A., 2021. Arclogites and their role in continental evolution; part 1: background, locations, petrography, geochemistry, chronology and thermobarometry. *Earth Sci. Rev.* 214, 103375.
- Dulnee, S., Banerjee, D., Merkel, B.J., Scheinost, A.C., 2013. Surface complexation and oxidation of Sn(II) by nanomagnetite. *Environ. Sci. Technol.* 47, 12852–12859.
- Durce, D., Salah, S., Van Laer, L., Wang, L., Maes, N., Brassinnes, S., 2022. Sn(IV) Sorption onto Illite and Boom Clay: Effect of Carbonate and Dissolved Organic Matter. *Minerals*, p. 1078.
- Fang, P., Luo, H., Xu, B., Huber, B.T., Zhu, Y., Mu, L., 2021. Planktic foraminifera of the upper Barremian-Aptian black shale intervals from the Chaqiela section (Gamba, southern Tibet): Biostratigraphic and palaeoenvironmental implications. *Cretaceous Res.* 127, 104934.
- Farges, F.O., Linnen, R.L., Brown Jr., G.E., 2006. Redox and speciation of tin in hydrous silicate glasses: a comparison with Nb, Ta, Mo and W. *Can. Mineral.* 44, 795–810.
- Frost, B.R., Shive, P.N., 1986. Magnetic mineralogy of the lower continental crust. *J. Geophys. Res.-Sol. Ea.* 91, 6513–6521.
- Gaschnig, R.M., Rudnick, R.L., McDonough, W.F., Kaufman, A.J., Valley, J.W., Hu, Z., Gao, S., Beck, M.L., 2016. Compositional evolution of the upper continental crust through time, as constrained by ancient glacial diamictites. *Geochim. Cosmochim. Acta* 186, 316–343.
- Gu, Z.Y., Lal, D., Liu, T.S., Guo, Z.T., Southon, J., Caffee, M.W., 1997. Weathering histories of Chinese loess deposits based on uranium and thorium series nuclides and cosmogenic ¹⁰Be. *Geochim. Cosmochim. Acta* 61, 5221–5231.
- Guo, Y., Li, Y., Deng, K., Wang, Z., Yang, S., 2024. Decoding the signals of sediment weathering: Toward a quantitative approach. *Chem. Geol.* 651, 122009.
- Han, C., Xiao, W., Su, B., Sakyi, P.A., Ao, S., Zhang, J., Zhang, Z., Wan, B., Song, D., Wang, Z., Zhao, N., 2018. Geology, Re-Os and U-Pb geochronology and sulfur isotope of the Donggebi porphyry Mo deposit, Xinjiang, NW China, Central Asian Orogenic Belt. *J. Asian Earth Sci.* 165, 270–284.
- Hanson, G.N., 1978. The application of trace elements to the petrogenesis of igneous rocks of granitic composition. *Earth Planet. Sci. Lett.* 38, 26–43.
- Hao, L.-L., Wang, Q., Kerr, A.C., Huang, F., Xiao, M., Ma, X.-L., Zhang, W.-F., Wang, W.-Y., Liu, M.-R., 2024. Andesitic arc magmas derived from two contrasting mélange origins: Evidence from central Tibetan dioritic porphyries. *Chem. Geol.* 650, 121920.
- Heinrich, C.A., 1990. The chemistry of hydrothermal tin-(tungsten) ore deposition. *Econ. Geol.* 85, 457–481.
- Holder, R.M., Yakymchuk, C., Viète, D.R., 2020. Accessory Mineral Eu Anomalies in Suprasolidus Rocks: Beyond Feldspar. *Geochem., Geophys., Geosyst.* 21, e2020GC009052.
- Hu, X., Nan, X., Liu, X., Huang, F., 2022. Rubidium isotope compositions of the average upper continental crust and the Himalayan leucogranites: implications for magmatic-fluid interaction. *Geochim. Cosmochim. Acta* 336, 165–176.
- Huang, S., Lin, C., Zhang, X., Zhang, N., 2021. Controls of diagenesis on the quality of shallowly buried terrestrial coarse-grained clastic reservoirs: a case study of the Eocene Shahejie Formation in the Damintun Sag, Bohai Bay Basin, Eastern China. *J. Asian Earth Sci.* 221, 104950.
- Huang, T.-Y., Teng, F.-Z., Rudnick, R.L., Chen, X.-Y., Hu, Y., Liu, Y.-S., Wu, F.-Y., 2020. Heterogeneous potassium isotopic composition of the upper continental crust. *Geochim. Cosmochim. Acta* 278, 122–136.
- Huang, F., Wang, J., Xiong, X., Gao, M., Li, L., Wei, C., 2024. Experimental determination of tin partitioning between titanite, ilmenite and granitic melts using improved capsule designs. *Am. Mineral.* in press.
- Irber, W., 1999. The lanthanide tetrad effect and its correlation with K/Rb, Eu/Eu*, Sr/Eu, Y/Ho, and Zr/Hf of evolving peraluminous granite suites. *Geochim. Cosmochim. Acta* 63, 489–508.
- Jian, X., Yang, S., Hong, D., Liang, H., Zhang, S., Fu, H., Zhang, W., 2020. Seasonal geochemical heterogeneity of sediments from a subtropical mountainous river in SE China. *Mar. Geol.* 422, 106120.
- Jiang, D.-S., Erdmann, S., Deng, G.-X., Guo, H.-H., Wu, F., Xu, X.-S., Xu, H., Zhao, Z.-F., Huang, F., 2022. Barium isotope evidence for the generation of peralkaline granites from a fluid-metasomatized crustal source. *Chem. Geol.* 614, 121197.
- Jochum, K.P., Hofmann, A.W., Seufert, H.M., 1993. Tin in mantle-derived rocks: Constraints on Earth evolution. *Geochim. Cosmochim. Acta* 57, 3585–3595.
- Jun, C., Junfeng, J., Gang, Q., Huayu, L., 1998. Geochemical studies on the intensity of chemical weathering in Luochuan loess-paleosol sequence, China. *Sci. China Ser. D Earth Sci.* 41, 235–241.
- Kemp, A.I.S., Hawkesworth, C.J., Paterson, B.A., Foster, G.L., Kinny, P.D., Whitehouse, M.J., Maas, R., Eimf, U., 2008. Exploring the plutonic-volcanic link: a zircon U-Pb, Lu-Hf and O isotope study of paired volcanic and granitic units from southeastern Australia. *Earth Environ. Sci. Trans. R. Soc. Edinb.* 97, 337–355.
- Klemme, S., Günther, D., Hametner, K., Prowatke, S., Zack, T., 2006. The partitioning of trace elements between ilmenite, ulvöspinel, armalcolite and silicate melts with implications for the early differentiation of the moon. *Chem. Geol.* 234, 251–263.
- Kröner, A., Hegner, E., Lehmann, B., Heinhorst, J., Wingate, M.T.D., Liu, D.Y., Ermelov, P., 2008. Palaeozoic arc magmatism in the Central Asian Orogenic Belt of Kazakhstan: SHRIMP zircon ages and whole-rock Nd isotopic systematics. *J. Asian Earth Sci.* 32, 118–130.
- Kubik, E., Siebert, J., Mahan, B., Creech, J., Blanchard, I., Agranier, A., Shcheka, S., Moynier, F., 2021. Tracing Earth's volatile delivery with tin. *J. Geophys. Res.-Sol. Ea.* 126, e2021JB022026.
- Kubik, E., Moynier, F., She, J.X., Rudnick, R.L., 2024. A baseline for the Sn isotopic composition of the upper continental crust. *Geochem. Perspect. Lett.* 30, 51–56.
- Kunz, B.E., Warren, C.J., Jenner, F.E., Harris, N.B.W., Argles, T.W., 2022. Critical metal enrichment in crustal melts: The role of metamorphic mica. *Geology* 50, 1219–1223.
- Larsen, L.M., 1979. Distribution of REE and other trace elements between phenocrysts and peralkaline undersaturated magmas, exemplified by rocks from the Gardar igneous province, south Greenland. *Lithos* 12, 303–315.
- Lee, C.-T., 2016. *Geochemical Classification of Elements*. In: White, W.M. (Ed.), *Encyclopedia of Geochemistry: A Comprehensive Reference Source on the Chemistry of the Earth*. Springer International Publishing, Cham, pp. 1–5.
- Lehmann, B., 2021. Formation of tin ore deposits: a reassessment. *Lithos* 402–403, 105756.
- Li, W., Jackson, S.E., Pearson, N.J., Alard, O., Chappell, B.W., 2009. The Cu isotopic signature of granites from the Lachlan Fold Belt, SE Australia. *Chem. Geol.* 258, 38–49.
- Li, W., Nakada, R., Takahashi, Y., Gaschnig, R.M., Hu, Y., Shakouri, M., Rudnick, R.L., Liu, X.-M., 2023. Cerium geochemical composition of the upper continental crust through time: Implications for tracing past surface redox conditions. *Geochim. Cosmochim. Acta* 359, 20–29.
- Li, W.-Y., Teng, F.-Z., Ke, S., Rudnick, R.L., Gao, S., Wu, F.-Y., Chappell, B.W., 2010. Heterogeneous magnesium isotopic composition of the upper continental crust. *Geochim. Cosmochim. Acta* 74, 6867–6884.
- Liu, P., Mao, J., Lehmann, B., Weyer, S., Horn, I., Mathur, R., Wang, F., Zhou, Z., 2021. Tin isotopes via fs-LA-MC-ICP-MS analysis record complex fluid evolution in single cassiterite crystals. *Am. Mineral.* 106, 1980–1986.
- Liu, S.-A., Rudnick, R.L., Liu, W.-R., Teng, F.-Z., Wu, T.-H., Wang, Z.-Z., 2023. Copper isotope evidence for sulfide fractionation and lower crustal foundering in making continental crust. *Sci. Adv.* 9, eadg6995.
- Liu, W.-M., Zheng, J.-P., Charlier, B., Ma, Q., Dai, H.-K., 2024. Genesis of the Devonian Habaqin ultramafic arc complex and associated low-grade Fe–Ti oxide mineralization in the northern North China Craton. *Lithos* 478–479.
- Luhr, J.F., Carmichael, I.S.E., 1980. The Colima Volcanic Complex, Mexico: I. Post-caldera andesites from Volcan Colima. *Contrib. Mineral. Petrol.* 71, 343–372.
- Luo, X.-L., Li, W., Du, D.-H., An, S., Zheng, B., Zhu, W., Xu, Z., 2024. Iron isotope systematics of the Jiajika granite-pegmatite lithium deposit, Sichuan, China. *Ore Geol. Rev.* 165, 105903.
- Mason, A.H., Powell, W.G., Bankoff, H.A., Mathur, R., Bulatović, A., Filipović, V., Ruiz, J., 2016. Tin isotope characterization of bronze artifacts of the central Balkans. *J. Archaeol. Sci.* 69, 110–117.
- Mason, A., Powell, W., Bankoff, H.A., Mathur, R., Price, M., Bulatović, A., Filipović, V., 2020. Provenance of tin in the Late Bronze Age Balkans based on probabilistic and spatial analysis of Sn isotopes. *J. Archaeol. Sci.* 122, 105181.
- Mathur, R., Powell, W., Mišta-Jakubowska, E., Duczko, W., Czech-Błońska, R., Błońska, M., Janowski, A., Żołędziowski, K., Jagodziński, M., Gójska, A., Kamenov, G., 2024. Isotopic metal compositions of Viking and medieval tin artifacts from Poland reveal expansive trade network. *J. Archaeol. Sci. Rep.* 53, 104296.
- Mazza, S.E., Gaschnig, R.M., Rudnick, R.L., Kleine, T., 2024. Tungsten stable isotope composition of the upper continental crust. *Geochim. Cosmochim. Acta* 370, 161–172.
- McLennan, S.M., 1993. Weathering and Global Denudation. *J. Geol.* 101, 295–303.
- Nan, X.-Y., Yu, H.-M., Rudnick, R.L., Gaschnig, R.M., Xu, J., Li, W.-Y., Zhang, Q., Jin, Z.-D., Li, X.-H., Huang, F., 2018. Barium isotopic composition of the upper continental crust. *Geochim. Cosmochim. Acta* 233, 33–49.
- Nesbitt, H.W., Young, G.M., 1982. Early Proterozoic climates and plate motions inferred from major element chemistry of lutites. *Nature* 299, 715–717.
- Peng, B., Song, Z., Tu, X., Xiao, M., Wu, F., Lv, H., 2004. Release of heavy metals during weathering of the Lower Cambrian Black Shales in western Hunan, China. *Environ. Geol.* 45, 1137–1147.
- Powell, W., Frchetti, M., Pulak, C., Bankoff, H.A., Barjamovic, G., Johnson, M., Mathur, R., Pigott, V.C., Price, M., Yener, K.A., 2022. Tin from Uluburun shipwreck shows small-scale commodity exchange fueled continental tin supply across Late Bronze Age Eurasia. *Sci. Adv.* 8, eabq3766.
- Romer, R.L., Kroner, U., 2015. Sediment and weathering control on the distribution of Paleozoic magmatic tin–tungsten mineralization. *Mineral Deposita* 50, 327–338.
- Romer, R.L., Kroner, U., 2016. Phanerozoic tin and tungsten mineralization—Tectonic controls on the distribution of enriched protoliths and heat sources for crustal melting. *Gondwana Res.* 31, 60–95.
- Romer, R.L., Kroner, U., Schmidt, C., Legler, C., 2022. Mobilization of tin during continental subduction-accretion processes. *Geology* 50, 1361–1365.
- Roskosz, M., Amet, Q., Fitoussi, C., Dauphas, N., Bourdon, B., Tissandier, L., Hu, M.Y., Said, A., Alatas, A., Alp, E.E., 2020. Redox and structural controls on tin isotopic fractionations among magmas. *Geochim. Cosmochim. Acta* 268, 42–55.
- Rudnick, R.L., 1995. Making continental crust. *Nature* 378, 571–578.
- Rudnick, R.L., Gao, S., 2003. 3.01 - Composition of the Continental Crust. In: Holland, H.D., Turekian, K.K. (Eds.), *Treatise on Geochemistry*. Pergamon, Oxford, pp. 1–64.
- Rudnick, R.L., Gao, S., 2014. 4.1 - Composition of the Continental Crust. In: Holland, H.D., Turekian, K.K. (Eds.), *Treatise on Geochemistry*, second ed. Elsevier, Oxford, pp. 1–51.

- Sauzéat, L., Rudnick, R.L., Chauvel, C., Garçon, M., Tang, M., 2015. New perspectives on the Li isotopic composition of the upper continental crust and its weathering signature. *Earth Planet. Sci. Lett.* 428, 181–192.
- She, J.-X., Kubik, E., Li, W., Moynier, F., 2023a. Stable Sn isotope signatures of Mid-ocean ridge basalts. *Chem. Geol.* 622, 121347.
- She, J.-X., Li, W., An, S., Cai, Y., 2023b. High-precision double-spike Sn isotope analysis of geological materials by MC-ICP-MS. *J. Anal. At. Spectrom.* 38, 142–155.
- She, J.-X., Li, W., An, S., Yang, T., Zhang, R., 2023c. In situ Sn isotope analysis of cassiterite (SnO₂) by nanosecond laser ablation MC-ICP-MS. *J. Anal. At. Spectrom.* 38, 1043–1056.
- Sillitoe, R.H., Lehmann, B., 2021. Copper-rich tin deposits. *Miner. Deposita* 57, 1–11.
- Stepanov, A.S., Allen, C.M., Jiang, S.-Y., Zhukova, I.A., Duan, D.-F., Wang, L., 2024. Geochemistry of metasedimentary restitic rocks and implications for melting conditions and metal potential of crustal felsic magmas. *Earth Sci. Rev.* 254, 104799.
- Stern, R.J., 2002. Subduction zones. *Rev. Geophys.* 40, 3-1-3-38.
- Sun, M., Mathur, R., Gao, C., Chen, Y., Yuan, S., 2023. Equilibrium Sn isotope fractionation between aqueous Sn and Sn bearing minerals Constrained by first principles calculations. *Am. Mineral.* 109, 265–273.
- Sun, S.S., McDonough, W.F., 1989. Chemical and isotopic systematics of oceanic basalts: implications for mantle composition and processes. *Geol. Soc. Lond. Spec. Publ.* 42, 313.
- Sun, K.-K., She, J.-X., Du, D.-H., Li, W., Deng, J., 2024. Extreme Sn isotope fractionation in highly evolved granites. *Chem. Geol.* 644, 121843.
- Sun, W.-D., Yang, X.-Y., Fan, W.-M., Wu, F.-Y., 2012. Mesozoic large scale magmatism and mineralization in South China: Preface. *Lithos* 150, 1–5.
- Taylor, S.R., McLennan, S.M., 1985. *The Continental Crust: Its Composition and Evolution*. *Geol. Mag.* 122, 673–674.
- Taylor, S.R., McLennan, S.M., McCulloch, M.T., 1983. Geochemistry of loess, continental crustal composition and crustal model ages. *Geochim. Cosmochim. Acta* 47, 1897–1905.
- Taylor, J.R., Wall, V.J., 1992. The behavior of tin in granitoid magmas. *Econ. Geol. Bull. Soc. Econ. Geol.* 87, 403–420.
- Telus, M., Dauphas, N., Moynier, F., Tissot, F.L.H., Teng, F.-Z., Nabelek, P.I., Craddock, P.R., Groat, L.A., 2012. Iron, zinc, magnesium and uranium isotopic fractionation during continental crust differentiation: the tale from migmatites, granitoids, and pegmatites. *Geochim. Cosmochim. Acta* 97, 247–265.
- Temizel, İ., 2013. Petrochemical evidence of magma mingling and mixing in the Tertiary monzogabbroic stocks around the Bafra (Samsun) area in Turkey: implications of coeval mafic and felsic magma interactions. *Miner. Petrol.* 108, 353–370.
- Teng, F.-Z., McDonough, W.F., Rudnick, R.L., Dalpé, C., Tomascak, P.B., Chappell, B.W., Gao, S., 2004. Lithium isotopic composition and concentration of the upper continental crust. *Geochim. Cosmochim. Acta* 68, 4167–4178.
- Teng, F.-Z., Dauphas, N., Helz, R.T., 2008. Iron isotope fractionation during magmatic differentiation in Kilauea Iki lava lake. *Science* 320, 1620–1622.
- Tian, S., Moynier, F., Inglis, E.C., Rudnick, R.L., Huang, F., Chauvel, C., Creech, J.B., Gaschnig, R.M., Wang, Z., Guo, J.-L., 2021. Zirconium isotopic composition of the upper continental crust through time. *Earth Planet. Sci. Lett.* 572, 117086.
- Wang, X., Amet, Q., Fitoussi, C., Bourdon, B., 2018. Tin isotope fractionation during magmatic processes and the isotope composition of the bulk silicate Earth. *Geochim. Cosmochim. Acta* 228, 320–335.
- Wang, X., Fitoussi, C., Bourdon, B., Fegley, B., Charnoz, S., 2019b. Tin isotopes indicative of liquid–vapor equilibration and separation in the Moon-forming disk. *Nat. Geosci.* 12, 707–711.
- Wang, X., Fitoussi, C., Bourdon, B., Richter, K., Amet, Q., 2021b. The Sn isotope composition of chondrites: implications for volatile element depletion in the Solar System. *Geochim. Cosmochim. Acta* 312, 139–157.
- Wang, Z.-Y., Luo, Z.-Y., Zhang, L., Liu, J.J., Li, J., 2022b. Sn Isotopic Values in Ten Geological Reference Materials by Double-Spike MC-ICP-MS. *Geostand. Geoanal. Res.* 46, 547–561.
- Wang, D., Mathur, R., Powell, W., Godfrey, L., Zheng, Y., 2019a. Experimental evidence for fractionation of tin chlorides by redox and vapor mechanisms. *Geochim. Cosmochim. Acta* 250, 209–218.
- Wang, T., She, J.-X., Yin, K., Wang, K., Zhang, Y., Lu, X., Liu, X., Li, W., 2021a. Sn(II) chloride speciation and equilibrium Sn isotope fractionation under hydrothermal conditions: a first principles study. *Geochim. Cosmochim. Acta* 300, 25–43.
- Wang, T., She, J.-X., Sun, Y., Li, Q., Lu, X., Li, W., Liu, X., 2023. Equilibrium Sn isotope fractionation among Sn-bearing minerals. *ACS Earth Space Chem.* 7, 2006–2018.
- Wang, Z.-Z., Teng, F.-Z., Wu, F.-Y., Liu, Z.-C., Liu, X.-C., Liu, S.-A., Huang, T.-Y., 2022a. Extensive crystal fractionation of high-silica magmas revealed by K isotopes. *Sci. Adv.* 8, eabo4492.
- Wang, R.C., Xie, L., Chen, J., Yu, A., Wang, L., Lu, J., Zhu, J., 2013. Tin-carrier minerals in metaluminous granites of the western Nanling Range (southern China): Constraints on processes of tin mineralization in oxidized granites. *J. Asian Earth Sci.* 74, 361–372.
- Wedepohl, K.H., 1995. The composition of the continental crust. *Geochim. Cosmochim. Acta* 59, 1217–1232.
- Wei, C., Xiong, X., Wang, J., Huang, F., Gao, M., 2024. Partitioning of tin between mafic minerals, Fe-Ti oxides and silicate melts: Implications for tin enrichment in magmatic processes. *Geochim. Cosmochim. Acta* 372, 81–100.
- Witt-Eickchen, G., Palme, H., O'Neill, H.S.C., Allen, C.M., 2009. The geochemistry of the volatile trace elements As, Cd, Ga, In and Sn in the Earth's mantle: New evidence from in situ analyses of mantle xenoliths. *Geochim. Cosmochim. Acta* 73, 1755–1778.
- Wu, F., Jahn, B.-M., Wilde, S.A., Lo, C.-H., Yui, T.-F., Lin, Q., Ge, W.-C., Sun, D.-Y., 2003. Highly fractionated I-type granites in NE China (I): geochronology and petrogenesis. *Lithos* 66, 241–273.
- Wu, J., Li, H., Mathur, R., Bouvier, A., Powell, W., Yonezu, K., Zhu, D., 2023. Compositional variation and Sn isotope fractionation of cassiterite during magmatic-hydrothermal processes. *Earth Planet. Sci. Lett.* 613, 118186.
- Wu, F., Liu, X., Ji, W., Wang, J., Yang, L., 2017. Highly fractionated granites: recognition and research. *Sci. China Earth* 60, 1201–1219.
- Wu, G., Zhu, J.-M., Wang, X., Johnson, T.M., He, Y., Huang, F., Wang, L.-X., Lai, S.-C., 2022. Nickel isotopic composition of the upper continental crust. *Geochim. Cosmochim. Acta* 332, 263–284.
- Xu, Z., Fu, X., Wang, R., Li, G., Zheng, Y., Zhao, Z., Lian, D., 2020. Generation of lithium-bearing pegmatite deposits within the Songpan-Ganze orogenic belt. *East Tibet. Lithos* 354–355.
- Xu, Z., Zheng, B., Zhu, W., Chen, Y., Li, G., Gao, J., Che, X., Zhang, R., Wei, H., Li, W., Wang, G., Wei, G., Yan, H., 2023. Geologic scenario from granitic sheet to Li-rich pegmatite uncovered by Scientific Drilling at the Jiajika lithium deposit in eastern Tibetan Plateau. *Ore Geol. Rev.* 161, 105636.
- Yao, J., Mathur, R., Powell, W., Lehmann, B., Tornos, F., Wilson, M., Ruiz, J., 2018. Sn-isotope fractionation as a record of hydrothermal redox reactions. *Am. Mineral.* 103, 1591–1598.
- Yi, W., Halliday, A.N., Lee, D.-C., Christensen, J.N., 1995. Indium and tin in basalts, sulfides, and the mantle. *Geochim. Cosmochim. Acta* 59, 5081–5090.
- Yuan, J., Hou, Q., Yang, Z., Jiang, H., Hu, Z., Yu, T., 2018. Distribution and mobilization of Sn in silicate minerals from the Mesozoic Shizhuoyuan W-dominated polymetallic deposit. *South China. Ore Geol. Rev.* 101, 595–608.
- Zhang, X., Chen, K., Hu, D., Sha, J., 2016. Mid-Cretaceous carbon cycle perturbations and Oceanic Anoxic Events recorded in southern Tibet. *Sci. Rep.* 6, 39643.
- Zhang, Z.-Z., Gu, L.-X., Wu, C.-Z., Shao, Y., Xu, J.-R., Zhai, J.-P., Zheng, Y.-C., Tang, J.-H., Wang, C.-S., San, J.-Z., 2008. Characteristics of source region and tectonic implications of Early Indosinian Weiyi gabbroic rock, eastern Tianshan mountains. *J. Cent. South Univ. Technol.* 15, 237–243.
- Zhang, G., Liu, Y., Moynier, F., Zhu, Y., Wang, Z., Hu, Z., Zhang, L., Li, M., Chen, H., 2020. Zinc isotopic composition of the lower continental crust estimated from lower crustal xenoliths and granulite terrains. *Geochim. Cosmochim. Acta* 276, 92–108.
- Zhang, H., Tian, S., Wang, D., Li, X., Liu, T., Zhang, Y., Fu, X., Hao, X., Hou, K., Zhao, Y., Qin, Y., 2021. Lithium isotope behavior during magmatic differentiation and fluid exsolution in the Jiajika granite–pegmatite deposit, Sichuan, China. *Ore Geol. Rev.* 134, 104139.
- Zhang, D., Zhou, T., Yuan, F., Fan, Y., Deng, Y., Xu, C., Zhang, R., 2014. Genesis of Permian granites along the Kangguer Shear Zone, Jueluotage area, Northwest China: geological and geochemical evidence. *Lithos* 198–199, 141–152.
- Zhao, P., Zajacz, Z., Tsay, A., Yuan, S., 2021. Magmatic-hydrothermal tin deposits form in response to efficient tin extraction upon magma degassing. *Geochim. Cosmochim. Acta* 316, 331–346.
- Zhou, Z.-H., Mao, J.-W., Zhao, J.-Q., Gao, X., Weyer, S., Horn, I., Holtz, F., Sossi, P.A., Wang, D.-C., 2022. Tin isotopes as geochemical tracers of ore-forming processes with Sn mineralization. *Am. Mineral.* 107, 2111–2127.
- Zhou, M., Zhang, R., Hanchar, J.M., Xu, Z., Lu, J., Hu, H., Che, X., Zheng, B., Li, G., 2023. Unravelling the genetic relationship between pegmatites and granites in the Jiajika Li-Be polymetallic district, Songpan-Ganze Orogenic Belt, Southwestern China: Insights from monazite U-Pb geochronology and trace element geochemistry. *Ore Geol. Rev.* 163, 105774.
- Zieman, L.J., Ibañez-Mejía, M., Tissot, F.L.H., Tompkins, H.G.D., Pardo, N., Bloch, E.M., 2024. Zirconium stable isotope fractionation during intra-crustal magmatic differentiation in an active continental arc. *Geochim. Cosmochim. Acta* 365, 53–69.